nature biomedical engineering

Article

https://doi.org/10.1038/s41551-025-01487-5

Fluid shear stress activates a targetable mechano-metastatic cascade to promote medulloblastoma metastasis

Received: 24 May 2024

Accepted: 18 July 2025

Published online: 02 September 2025

Check for updates

Hyun-Kee Min[1,2,3,17], Hongyu Zhao[1,2,4,5,17], Alexander Bahcheli[3,6], Peng Pan[7,8], Jade Chan[1,2,3], Junsheng Chen[1,2], Esther Low[1,2], Yuxiao Zhou[7], Xian Wang[1,2,9,10], Savo Bajic[7], Ran Peng[11], Siyi Wanggou[1,2,4,5], Qi Yang[1,2], Robert Du Yang Zhang[1,2], Leiming Wang[12], Xiufang Ren[13], Haoyue Qi[14], Yu Shi[14], Madeline N. Hayes[1,3], Brian Ciruna[1,3], Jüri Reimand[3,6,15], Xinyu Liu[7,16] & Xi Huang[1,2,3] ✉

Biofluid flow generates fluid shear stress (FSS), a mechanical force widely present in the tissue microenvironment. How brain tumour growth alters the conduit of biofluid and impacts FSS-regulated cancer progression is unknown. Dissemination of medulloblastoma (MB) cells into the cerebrospinal fluid initiates metastasis within the central nervous system. Here, by simulating cerebrospinal fluid dynamics based on magnetic resonance imaging of patients with MB, we discover that FSS is elevated at the cervicomedullary junction. MB-relevant FSS promotes metastasis along the mouse spinal cord. Mechanistically, FSS induces metastatic cell behaviours, including weakened cell-substrate adhesion, increased motility, cell clustering and plasma membrane localization of glucose transporter 1 (GLUT1) to enhance glucose uptake. FSS is perceived by the mechanosensitive ion channel PIEZO2, which drives actomyosin contractility-dependent GLUT1 recruitment at the plasma membrane. Genetic targeting of PIEZO2 or pharmacologic inhibition of GLUT1 mitigates metastasis. Collectively, these findings define a targetable FSS-activated mechano-metastatic cascade for the treatment of MB metastasis.

Cancer metastasis accounts for up to 90% of cancer deaths[1]. The tumour microenvironment generates diverse signals to dictate the metastatic potential of tumour cells. Compared with the large body of knowledge of the genetic underpinnings and biochemical pathways that regulate metastasis, the reciprocal interactions between tissue mechanics and cancer progression are poorly understood. Fluid shear stress (FSS), solid stress and tissue biomaterial properties (that is, stiffness, elasticity and viscosity) constitute the mechanical tissue microenvironment. Owing to uncontrolled cell proliferation within geometrical confinement, stromal and immune cell infiltration, dysregulated extracellular matrix and perturbed biofluid flow, cancer cells experience a myriad of mechanical cues[2–4]. These mechanical stimuli impact tumour proliferation, invasion, angiogenesis and therapy response[5–21].

Metastasis is a multi-step process in which tumour cells mobilize within the primary tumour, invade tumour stroma and surrounding tissue, intravasate and extravasate blood vessels, and anchor at distant sites for initial dormancy and subsequent metastatic outgrowth. During these events, tumour cells perceive the stiffness of extracellular matrix (ECM), experience compressive stress as they squeeze through the endothelium, and sense FSS generated by the flow of blood, lymph, interstitial fluid or cerebrospinal fluid (CSF)[22,23]. Tissue stiffening can promote metastasis by driving epithelial–mesenchymal transition[24,25]. Confined tumour cell migration upregulates inhibitors of apoptosis (IAPs) to confer anoikis resistance to enhance metastasis[26]. A blood flow shear stress optimum determines where circulating tumour cells arrest and extravasate, which influences metastatic success[27]. While these studies revealed the

A full list of affiliations appears at the end of the paper. ✉e-mail: xi.huang@sickkids.ca

https://doi.org/10.1038/s41551-025-01487-5

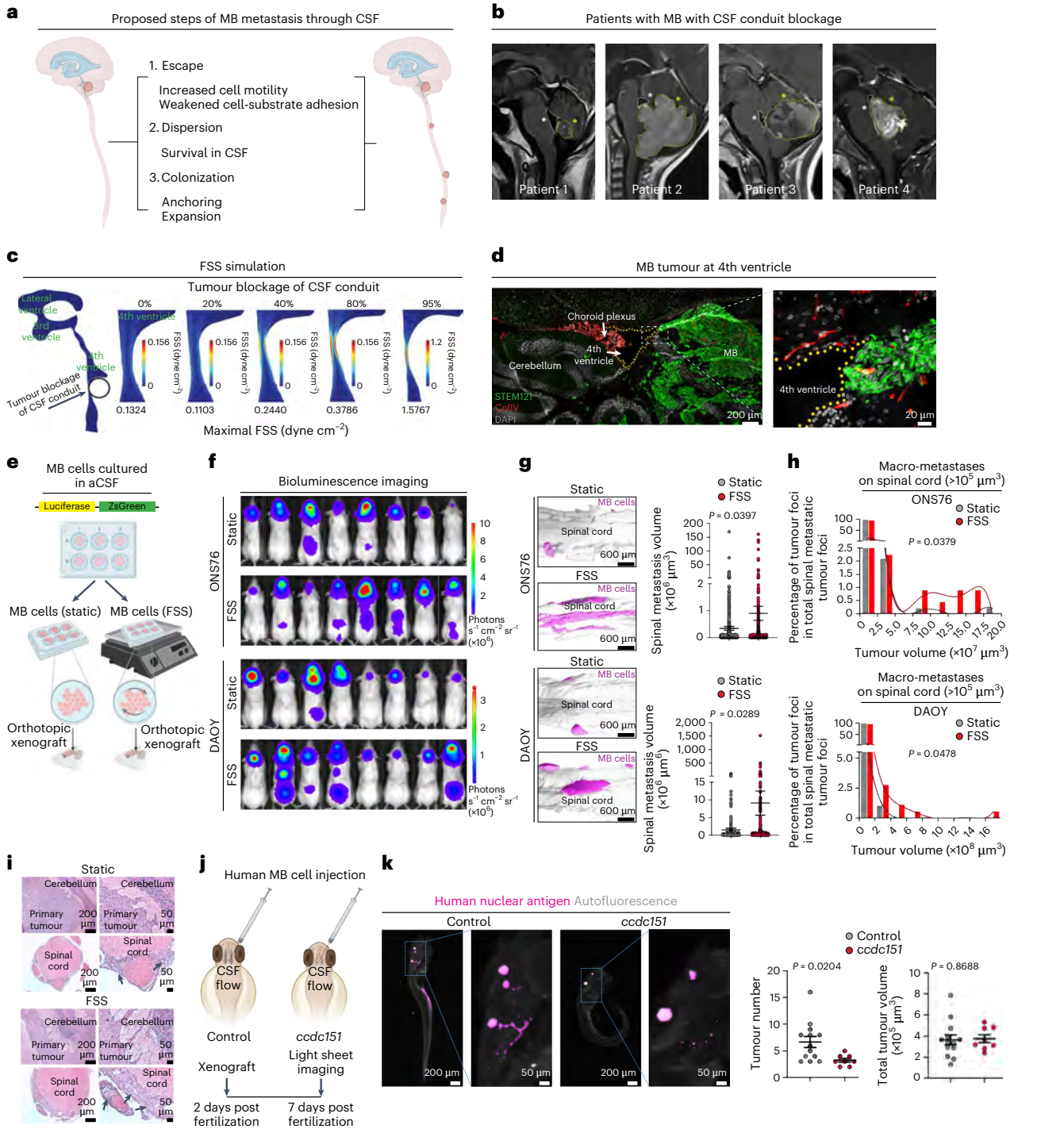

Fig. 1 | MB tumour obstruction of the CSF conduit elevates FSS to promote metastasis. a, Proposed steps of MB metastasis through CSF. **b**, MRIs of MB tumours that block CSF conduit in patients. The white and yellow asterisks and outlines represent the fourth ventricle and the MB tumour, respectively. **c**, Computational simulation of CSF shear stress with various levels of MB blockage of the CSF conduit. **d**, Immunostaining detects MB cells, which express the human-specific antigen STEM121, and blood vessels labelled by Collagen IV (ColIV). Tumour cells can be seen in direct contact of the 4th ventricle. **e**, Experimental set-up for using static control or FSS-treated MB cells for orthotopic xenograft. **f**, Bioluminescence images of xenograft tumours derived from static control or FSS-treated MB cells at 42 days (ONS76) and 49 days (DAOY) post implantation. Images are from $n = 8$ mice across two or three independent xenograft experiments for ONS76 or DAOY, respectively. **g**, Metastatic tumours along the spinal cords of mice bearing xenograft tumours derived from static control or FSS-treated MB cells. 3D reconstructions of the spinal cords (autofluorescence) and tumours (ZsGreen) are shown. Graphs show quantifications of spinal metastasis volume of $n = 2,692$ metastatic tumours from 6 mice (ONS76 static), $n = 1,248$ tumours from 5 mice (ONS76 FSS), $n = 396$ tumours from 3 mice (DAOY static) and $n = 505$ tumours from 3 mice (DAOY FSS). *P* values, two-sided Welch's *t*-test. Error bars, mean ± s.e.m. **h**, Quantifications of the volume distribution of spinal macro-metastases in the control and FSS groups. Histograms with nonlinear regression curves are shown. $n = 478$ macro-metastases from 6 mice (ONS76 static), $n = 223$ macro-metastases from 5 mice (ONS76 FSS), $n = 96$ macro-metastases from 3 mice (DAOY static) and $n = 179$ macro-metastases from 3 mice (DAOY FSS). *P* values, two-sided Welch's *t*-test. **i**, Haematoxylin-and-eosin staining images of primary and metastatic MB. The grey arrows represent MB metastases. **j**, Schematic for MB xenograft into control or *ccdc151* CSF flow defective zebrafish. **k**, *ccdc151* xenografts have reduced tumour number. Graphs represent results from $n = 13$ (control) and $n = 8$ (ccdc151) zebrafish. *P* value, two-sided unpaired *t*-test. Error bars, mean ± s.e.m. Schematics in **a**, **e** and **j** were created using BioRender.com.

importance of mechanical signals during cancer metastasis, the molecular sensors of mechanical signals, the force-activated signalling pathways leading to metastatic cell behaviours, and the therapeutic targetability of the mechanotransduction events remain poorly understood.

Medulloblastoma (MB) is the most common malignant paediatric brain tumour[28,29]. MB comprises four subgroups (SHH, WNT, Group 3 and Group 4), each with distinct cells of origin, genetic mutations, epigenetic features and clinical outcomes[28]. Despite these differences, metastasis occurs in all subgroups[30,31]. MB cells disseminate into the CSF and blood[31–33] and metastasize throughout the CSF conduit, including brain ventricles, central canal of the spinal cord and the leptomeningeal space of the central nervous system (CNS). MB metastasis through the CSF is proposed to occur through the leptomeningeal dissemination (LMD) cascade[31]. In the LMD, MB cells escape from primary tumour by gaining enhanced motility and weakened cell-substrate adhesion, survive in the nutrient-scarce CSF and disperse throughout the brain ventricles and leptomeninges, and establish leptomeningeal colonization (Fig. 1a). Metastatic MB tumours along the spinal cord are chemorefractory and unresectable, conferring an especially poor prognosis to patients. This clinical observation highlights the urgent need to develop therapies that target the molecular vulnerabilities of disseminated MB cells. However, owing to the scarcity of resected samples, genetic heterogeneity and lack of robust imaging approaches to detect metastatic tumours at cellular resolution, MB metastasis is rarely studied[32,34,35]. NOTCH1 signalling and γ-aminobutyric acid (GABA) metabolism have been identified to regulate MB metastasis[36,37], but a deeper understanding of the mechanisms is required to identify therapeutic targets. Of the diverse mechanical stimuli that MB cells experience, FSS is of particular relevance owing to the flow of CSF[38,39]. In patients, MB infiltrates into the 4th ventricle floor and 4th ventricle infiltration portends poor patient outcomes[40]. However, whether FSS contributes to MB metastasis is completely unknown.

Here we show that MB growth leads to CSF conduit blockage at the cervicomedullary junction, thereby elevating CSF flow and FSS. MB-relevant FSS promotes MB metastasis by inducing an amoeboid-like tumour cell state with increased motility, weakened cell-substrate adhesion, cell clustering and glucose transporter 1 (GLUT1)-mediated glucose uptake. These effects are driven by the FSS-activated PIEZO2-actomyosin-GLUT1 signalling cascade, which can be genetically or pharmacologically targeted to mitigate MB metastasis. These findings unveil a mechanically activated metastatic mechanism and molecular vulnerabilities, which can be leveraged to develop targeted therapies to treat MB.

Results

CSF conduit blockage by MB elevates CSF flow

Patients with MB exhibit 4th ventricle compression and hydrocephalus owing to physical blockage of CSF conduit by the tumour bulk[41,42]. However, the precise site of CSF conduit blockage and how MB-induced abnormality affects CSF flow is undetermined. To determine CSF FSS in patients with MB, we created a boundary model of the ventricular system based on previously defined CSF conduit geometries[43]. We analysed magnetic resonance images (MRIs) of ten patients with MB where we observed a wide range of CSF conduit constriction by the tumour bulk. The cervicomedullary junction was the most common site of constriction (Fig. 1b, Extended Data Fig. 1a and Supplementary Table 1). On the basis of this finding, we applied varying degrees of tumour-induced constriction at the cervicomedullary junction to the CSF conduit boundary model. Using COMSOL, we performed finite element simulation of CSF FSS and flow rate with 0–95% blockage of the CSF conduit[43,44]. Our simulation reveals that the maximum FSS on the cervicomedullary junction wall is ~0.13 dyne cm^{-2} in the unconstricted state (Fig. 1c). The maximum FSS is elevated to ~0.24 dyne cm^{-2} with 40% constriction to ~1.58 dyne cm^{-2} with 95% constriction. Consistently, the maximal flow velocity is ~18.4 mm s^{-1} in the unconstricted state and elevated to ~48.1 mm s^{-1} with 95% constriction (Extended Data Fig. 1b). Since tumour-induced constriction may raise pressure within the ventricular system, we also measured pressure levels and observed that from 20% to 95% constriction, pressure increases around 4-fold (Extended Data Fig. 1c), while FSS increases around 14-fold (Fig. 1c). These findings suggest that FSS appears to be a dominant mechanical stimulus of the MB microenvironment impacted by the tumour bulk. MB tumour cells, which were traced by their expression of human-specific antigen STEM121, were detected to be in direct contact of the 4th ventricle in an orthotopic xenograft model of MB derived from ONS76 cells (Fig. 1d). Collectively, these results present the estimated range of FSS within the MB-bearing human ventricular system through a computational model based on patient MRIs and show that tumour cells can be positioned to perceive the FSS generated by CSF flow in mice.

FSS promotes MB metastasis

Having determined that FSS is conspicuously elevated owing to MB-induced CSF conduit blockage, we asked: does FSS functionally regulate MB metastasis? To determine the effects of FSS, we cultured firefly luciferase- and ZsGreen-expressing MB cells in artificial CSF (aCSF), which mimics the nutrient-scarce condition of human CSF (Methods). Guided by the range of FSS derived from the computational simulation, we treated MB cells with disease-relevant level of FSS (Fig. 1e): MB cells were subjected to 18 h of orbital shaking that produces a maximal FSS of ~0.35–0.4 dyne cm^{-2} (Supplementary Video 1), which is in line with 80–95% CSF conduit blockage (Fig. 1c). We orthotopically xenografted FSS-treated or static control MB cells into immunodeficient NOD SCID gamma mice. Non-invasive bioluminescence imaging (BLI) revealed that xenograft mice in the FSS group exhibited increased incidence of metastatic tumours along the spinal cord compared with the static control group in two human MB cell models, ONS76 (2/8 mice of the static control group, 5/8 mice in the FSS group) and DAOY (1/8 mice of the static control group, 4/8 mice in the FSS group) (Fig. 1f). To quantitatively compare spinal cord metastases, we collected the entire spinal cords from tumour-bearing mice at endpoint, subjected the spinal cords to optical clearing using the CUBIC technique[45] and performed laser scanning confocal microscopy. Of note, we report for the first time the use of optical clearing coupled with three-dimensional (3D) reconstruction to visualize metastatic tumours on spinal cords (Methods). This method possesses sufficient resolution to detect macro-metastases (which we defined as foci $>10^5$ μm^3), micro-metastases (foci $<10^5$ μm^3) and single cells, permitting high precision inquiries into spinal cord metastasis. In both ONS76 and DAOY orthotopic xenograft models, the average volume of spinal cord metastases was over twofold larger in the FSS group compared with the static control group (Fig. 1g,i). FSS significantly increased the abundance of macro-metastases (Fig. 1h). To further determine whether in vivo FSS impacts MB metastasis, we performed MB xenografts using control and CSF flow-defective zebrafish. Zebrafish xenograft tumours exhibit comparable proliferation, histology and chemosensitivity to mouse xenograft tumours[46]. Human MB cells engraft and form tumours in zebrafish larvae[47]. Owing to defects in motile cilia beating, the *ccdc151* mutant zebrafish show defective and slower CSF flow compared with control zebrafish[48–50]. We injected MB cells into the hindbrain of control or *ccdc151* mutant zebrafish, performed tissue clearing of the tumour-bearing fish 5 days post injection and performed light sheet imaging to compare tumour burdens and distributions (Fig. 1j). We found that while the overall MB tumour burdens are comparable, *ccdc151* mutant zebrafish show significantly decreased tumour numbers (mean ± s.e.m. control, 6.692 ± 1.034; *ccdc151*, 3.250 ± 0.366) as an indicator of metastatic dissemination (Fig. 1k). Collectively, these results show that disease-relevant magnitudes of FSS promote MB metastasis.

FSS induces an amoeboid-like state of MB cells

Since FSS increased the metastatic potential of MB cells, we investigated whether FSS induces cell behaviours related to the LMD

https://doi.org/10.1038/s41551-025-01487-5

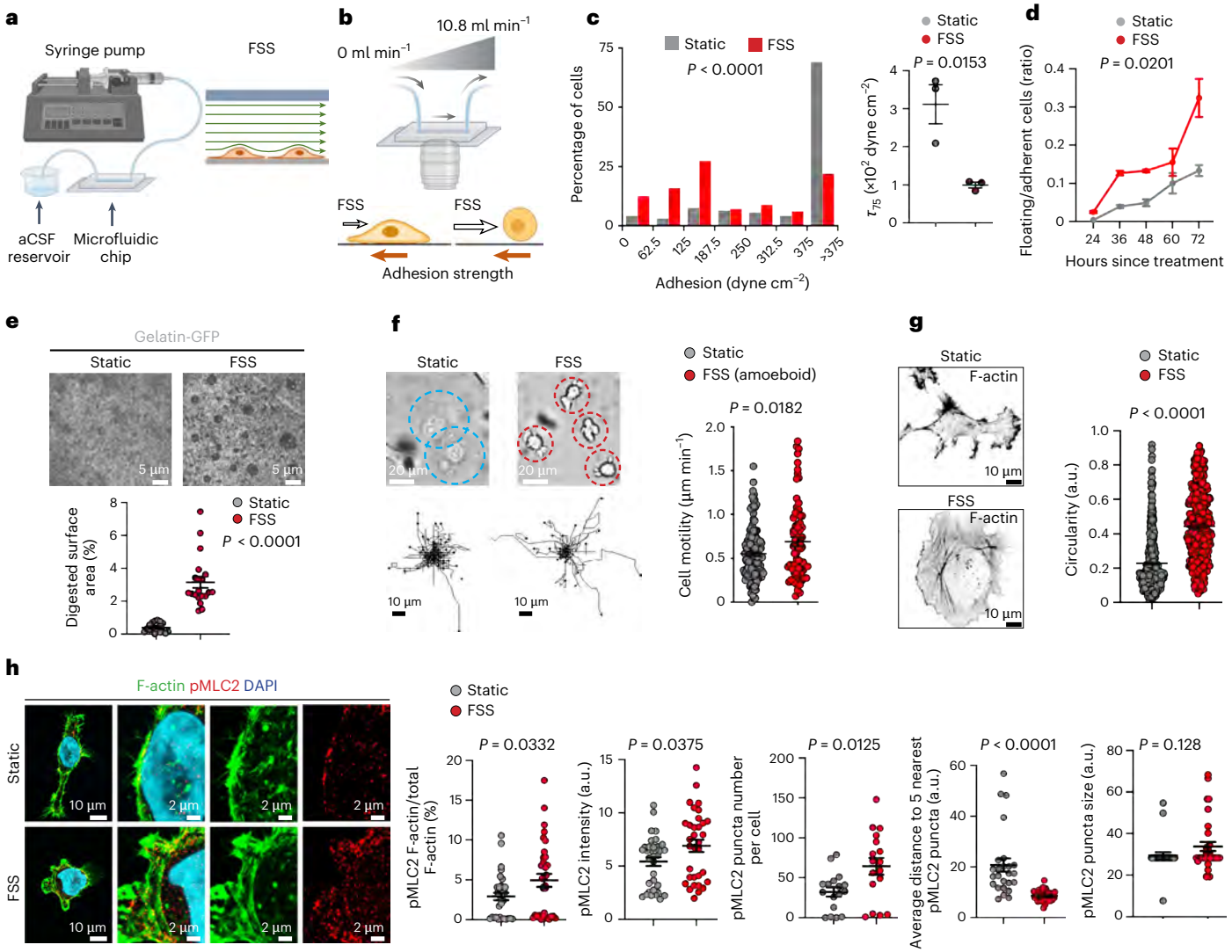

Fig. 2 | FSS weakens MB cell-substrate adhesion, increases cell motility and promotes actomyosin contractility. a, Microfluidic device for FSS application to MB cells. **b**, Experimental set-up for determining MB cell-substrate adhesion strength. **c**, Left: cell-substrate adhesion of static control or FSS-treated ONS76 cells. Histograms represent results from $n = 266$ cells (static) and $n = 295$ cells (FSS) from three independent replicates. *P* value, one-sided chi-square test. Right: τ_{75} results of the three independent replicates are shown. *P* value, two-sided unpaired *t*-test. Error bars, mean ± s.e.m. **d**, Quantification of the ratio of floating/adherent ONS76 cells in the static control or FSS-treated group. The graph represents results from three independent replicates ($n = 3$). *P* value, two-way analysis of variance. Error bars, mean ± s.e.m. **e**, ECM degradation ability of static control or FSS-treated ONS76 cells. The graph shows quantifications of digested gelatin-GFP area per field of view. $n = 20$ fields of view from three independent replicates. *P* value, two-sided unpaired *t*-test. Error bars, mean ± s.e.m. **f**, Morphology and motility of static control or FSS-treated ONS76 cells. The blue dashed circles show the mesenchymal-like cell morphology of ONS76 under static condition. The red dashed circles show the amoeboid-like cell morphology of ONS76 under FSS condition. The graph shows quantifications of cell velocity of $n = 139$ (static) and $n = 73$ (FSS) cells from three independent replicates. *P* value, two-sided unpaired *t*-test. Error bars, mean ± s.e.m. **g**, FSS-treated ONS76 cells have increased circularity. Immunofluorescence of F-actin was performed on static control and FSS-treated ONS76 cells. The graph represents results of $n = 389$ (static) and $n = 419$ (FSS) cells from three independent replicates. *P* value, two-sided unpaired *t*-test. Error bars, mean ± s.e.m. **h**, Actomyosin contractility of static control or FSS-treated ONS76 cells. Graphs show quantifications of pMLC2 coverage of F-actin, pMLC2 intensity on F-actin, pMLC2 puncta number on F-actin, distance between pMLC2 puncta and pMLC2 puncta size. pMLC2 coverage and intensity are from $n = 34$ (static) and $n = 33$ (FSS) cells. The pMLC2 puncta number is from $n = 17$ (static, FSS) cells. The pMLC2 puncta distance and size are from $n = 25$ (static) and $n = 33$ (FSS) cells. All results are from three independent replicates. *P* value, two-sided unpaired *t*-test. Error bars, mean ± s.e.m. Schematics in **a** and **b** were created using BioRender.com.

cascade (Fig. 1a). To enable live imaging of cells under fluid flow, we custom-built microfluidic channels within which MB cells were treated with ~0.5 dyne cm^{-2} of FSS for 6 h (Fig. 2a). As a control, cells were cultured in the microfluidic channels without FSS. After ensuring that sterilization did not deform the microfluidic channels (Extended Data Fig. 2a), first, we studied whether FSS alters MB cell-substrate adhesion strength. To this end, we used an established assay[51,52], where a gradient of fluid flow was applied to the ~0.5 dyne cm^{-2} FSS-treated or static control cells over a fixed period to shear the cells off their substrate. Simultaneously, live imaging was performed so that the number of cells detaching, and at which fluid flow level, could be quantified. Since cells detach at the point where fluid flow exceeds the adhesion strength, the fluid flow level at which a cell detaches is a measure of that cell's adhesion strength (Fig. 2b). Histograms show the distribution of adhesion strengths for the sheared off cells and cells that remained attached after the fluid flow gradient (>375 dyne cm^{-2}), and τ_{75} shows the gradient shear stress at which 25% of the cells detached[53–55] (Fig. 2c and Extended Data Fig. 2b). FSS-treated cells were significantly less adherent than the static

https://doi.org/10.1038/s41551-025-01487-5

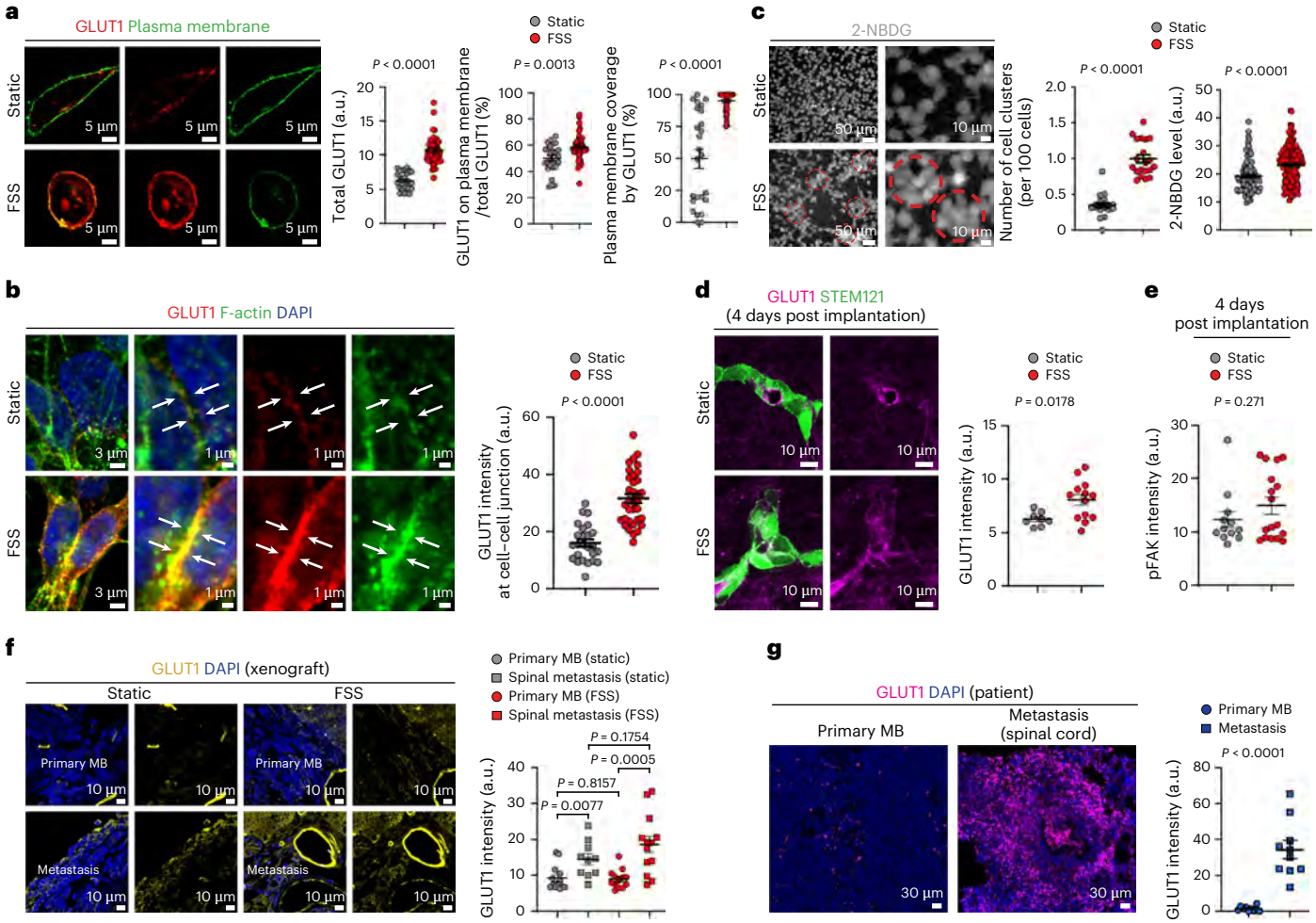

Fig. 3 | FSS promotes plasma membrane localization of GLUT1 and glucose uptake. a, GLUT1 localization in individual static or FSS-treated ONS76 cells. Graphs show total GLUT1 level, percentage of GLUT1 on the plasma membrane and percentage coverage of the plasma membrane by GLUT1 from $n = 25$ (static) and $n = 46$ (FSS) cells from three independent replicates. *P* value, two-sided unpaired *t*-test. Error bars, mean ± s.e.m. **b**, GLUT1 intensity at cell–cell junctions of static or FSS-treated ONS76 cells. The white arrows point to the cell–cell junction. The graph represents results from $n = 25$ (static) and $n = 34$ (FSS) cell–cell junctions from three independent replicates. *P* value, two-sided unpaired *t*-test. Error bars, mean ± s.e.m. **c**, Glucose uptake and cell clustering ability of static or FSS-treated ONS76 cells. The red dashed circles represent the cell clusters. Graphs show the number of cell clusters per 100 cells from $n = 20$ fields of view from three independent replicates (left) and 2-NBDG level in each cell from $n = 94$ (static) and $n = 159$ (FSS) cells from three independent replicates (right). *P* value, two-sided unpaired *t*-test. Error bars, mean ± s.e.m. **d**, GLUT1 is elevated in FSS-treated MB xenograft tumours 4 days post implantation. The graph shows GLUT1 signal in STEM121$^+$ tumour cells in $n = 8$ fields of view from 3 mice (static) and $n = 13$ fields of view from 4 mice (FSS). *P* value, two-sided unpaired *t*-test. Error bars, mean ± s.e.m. **e**, pFAK levels are comparable in static and FSS-treated xenografts at 4 days post implantation. The graph shows the pFAK signal in STEM121$^+$ tumour cells in $n = 12$ fields of view from 3 mice (static) and $n = 17$ fields of view from 4 mice (FSS). *P* value, two-sided unpaired *t*-test. Error bars, mean ± s.e.m. **f**, GLUT1 expression in primary ONS76 xenograft tumours and spinal metastases from static or FSS-treated cells. The graph shows tumour GLUT1 intensity from $n = 13$ (static primary MB, FSS primary MB, FSS metastasis) and $n = 10$ (static metastasis) fields of view from 3 (static primary MB), 3 (static metastasis), 4 (FSS primary MB) and 3 (FSS metastasis) mice. *P* value, two-sided unpaired *t*-test. Error bars, mean ± s.e.m. **g**, GLUT1 expression in primary patient MB and metastasis. The graph shows GLUT1 intensity in a patient's matched primary MB and metastasis biopsies from 10 fields of view. *P* value, two-sided unpaired *t*-test. Error bars, mean ± s.e.m.

control cells both on poly-L-lysine (Fig. 2c) and RGD peptide (Extended Data Fig. 2b) substrates. To corroborate this finding, we subjected MB cells to orbital shaking that generates ~0.35–0.4 dyne cm^{-2} FSS or static culture on laminin-coated dishes. The ratio of floating to adherent MB cells was significantly increased over time in the FSS group compared with the static control group (Fig. 2d). To further characterize the effects of FSS on cell adhesion, we determined the expression of selectin ligands, which bind to selectins expressed on vascular endothelial cells, leukocytes and platelets[56] to regulate circulating tumour cell adhesion to the vascular endothelium[57]. P-selectin glycoprotein ligand 1 (PSGL1), E-selectin ligand 1 (ESL1) and major E-selectin ligand CD44[58,59] expression increased, did not alter and decreased in FSS-treated cells, respectively (Extended Data Fig. 2c). These results show that FSS has a complex impact on the expression of selectin ligand, and warrant future studies into the role of selectins in MB metastasis. Second, we studied whether FSS influences the ability of MB cells to degrade the ECM. To this end, we cultured MB cells on gelatin-GFP-coated substrate and then subjected them to orbital shaking or static culture. FSS enhanced the ability of MB cells to degrade gelatin-GFP compared with the static control group (Fig. 2e and Extended Data Fig. 2d). Third, we studied whether FSS impacts MB cell motility. Using live imaging, we observed that FSS treatment led to an amoeboid-like cell morphology, including cell rounding and blebbing[60] (Fig. 2f,g). FSS-treated DAOY cells and ONS76 cells exhibiting amoeboid movement showed increased motility compared with static control cells (Fig. 2f and Extended Data Fig. 2e). Actomyosin contraction, facilitated by phosphorylation of

myosin light chain 2 (pMLC2), promotes amoeboid movement and heightened motility[60,61]. FSS-treated MB cells showed increased F-actin coverage by pMLC2, elevated pMLC2 intensity, more pMLC2 puncta per cell and decreased distance between these puncta, indicating that FSS promotes actomyosin contractility (Fig. 2h). Amoeboid cells are characterized by rounded morphology, high actomyosin contractility, low substrate adhesion and blebs as functional protrusions that enable fast migration[60]. Altogether, these findings show that FSS induces an amoeboid-like state in MB cells, which confers cellular behaviours essential for the 'escape' step of the LMD cascade.

FSS increases plasma membrane GLUT1 and glucose uptake

CSF is a nutrient-scarce microenvironment with a protein concentration ~100 times lower than blood[62]. CSF is largely acellular with less than 5 mononuclear cells per millilitre[63]. Furthermore, CSF glucose concentration is approximately two-thirds that of the blood[64], raising the question of how disseminated MB cells survive in the CSF. In kidney and breast epithelial cells, FSS was shown to induce cell–cell junctional enrichment of GLUT1 in an actomyosin contraction-dependent manner[65]. As such, we investigated GLUT1 in FSS-treated and static control MB cells. FSS increased the overall GLUT1 level, the proportion of GLUT1 on the plasma membrane, the percentage of the plasma membrane covered by GLUT1 (Fig. 3a) and GLUT1 levels at MB cell–cell junctions (Fig. 3b and Extended Data Fig. 2f). Consistently, FSS increased the intracellular level of fluorescent glucose analogue 2-NBDG, as well as cell clustering (Fig. 3c and Extended Data Fig. 2g). To determine whether increased substrate stiffness phenocopies FSS, we cultured MB cells on polyacrylamide gels of MB-relevant stiffness (500 Pa and 5,000 Pa)[66]. Cell–cell junctional GLUT1 levels were reduced by around 10% in stiffer substrate (5,000 Pa) compared with softer substrate (500 Pa) (Extended Data Fig. 2h), suggesting that in MB cells, substrate stiffness increase does not phenocopy FSS treatment. Next, we sought to determine the duration of phenotypic alterations induced by FSS in vitro and in vivo. For in vitro, we compared cell–cell junctional GLUT1 and actomyosin contraction of static and FSS-treated MB cells at 2 h, 6 h and 24 h post FSS withdrawal. FSS-induced GLUT1 cell–cell junctional enrichment persisted up to 6 h post FSS withdrawal, while actomyosin contraction persisted up to 2 h (Extended Data Fig. 2i). For in vivo, we studied GLUT1 levels in tumour cells of static and FSS-treated MB xenografts at 4 days post injection. GLUT1 levels were significantly higher in FSS-treated xenografts compared with static control (Fig. 3d). Together, these data show that MB cells display 'mechanical memory' of the FSS and exhibit cellular changes that last hours to days depending on their microenvironment (that is, in vitro culture condition versus in vivo cerebellum tissue). Given that we observed reduced cell-substrate adhesion and increased motility of FSS-treated MB cells (Fig. 2c,d,f and Extended Data Fig. 2b,e), we examined whether at 4 days post injection, FSS-treated xenografts have altered substrate adhesion and tumour spread. Focal adhesion kinase (FAK) is phosphorylated upon cell adhesion to ECM proteins[67,68]. Thus, pFAK is used as a marker for cell-substrate adhesion in tissues[69,70]. We quantified tumour spread by measuring solidity, which is the ratio of the tumour area (marked by STEM121) to the area of the tumour convex hull. As such, low solidity indicates a more disperse and spread-out tumour. We observed no significant difference in pFAK levels (Fig. 3e) or tumour spread (Extended Data Fig. 2j) between static and FSS-treated xenografts, suggesting that FSS-treated MB cells do not develop lower cell-substrate adhesion or wider spread at early time point after implantation. In endpoint xenografts, while metastatic MB cells in the spinal cords had comparable circularity to primary tumour cells (Extended Data Fig. 2k), they exhibited higher GLUT1 expression in both static and FSS-treated MB xenografts (Fig. 3f). Furthermore, in matched patient primary MB and spinal metastasis tissue biopsies, GLUT1 levels were significantly higher in the metastasis compared with primary tumour (Fig. 3g), demonstrating an association between high GLUT1 levels and metastatic success. These data show that FSS promotes GLUT1-mediated glucose uptake that may be critical for metastatic success.

To determine the impact of FSS on MB cell transcriptome, we performed bulk RNA-seq of static control and FSS-treated MB cells. Consistent with the finding that FSS-treated MB cells show increased ability to degrade the ECM (Fig. 2e and Extended Data Fig. 2d), pathway enrichment analysis of the differentially expressed genes (DEGs) reveals altered 'metallopeptidase activity', 'endopeptidase activity' and 'serine-type peptidase activity' in FSS-treated ONS76 cells (Extended Data Fig. 2l). Consistent with the finding that FSS-treated MB cells show increased cell motility (Fig. 2f and Extended Data Fig. 2e), the enriched pathways include 'leukocyte migration' and 'wound healing' in FSS-treated DAOY cells (Extended Data Fig. 2l). Furthermore, pathway enrichment analysis highlights specific cellular processes and signalling pathways, such as 'ATP-dependent protein folding chaperone' and 'regulation of trans-synaptic signalling' (Extended Data Fig. 2l). Given the reported roles of protein chaperones in facilitating metastatic tumour cells to cope with cellular stress[71] and neuron–tumour cell synaptic signalling in promoting brain metastasis[72], these RNA-seq and pathway enrichment data can serve as useful resources for future investigation of MB metastasis mechanisms.

FSS activates the PIEZO2-actomyosin-GLUT1 signalling cascade

Next, we sought to determine the molecular sensor of FSS in MB cells. Mechanosensitive ion channels perceive mechanical force to permeate cations, such as calcium, which activates intracellular signalling[3]. We surveyed the expression of force-activated ion channels[3], including mechanosensitive potassium, sodium and non-selective cation channels, in primary non-metastatic MB and metastatic MB based on the Cavalli et al. human MB RNA sequencing dataset[73]. PIEZO2, a

Fig. 4 | FSS activates PIEZO2 to increase intracellular calcium and actomyosin contractility, which elevates GLUT1 localization at plasma membrane and glucose uptake. a, *PIEZO2* expression from $n = 134$ non-metastatic and $n = 26$ metastatic SHH MB patients. *P* value, two-sided Mann–Whitney *U*-test. Box plots indicate interquartile range (IQR; 25th–75th percentiles) with median and 1.5 × IQR whiskers. **b**, Representative calcium traces of FSS-treated MB cells. **c**, Maximum calcium amplitudes within active compartments. $n = 74$ compartments across 20 cells (ONS76 nt. shRNA), $n = 33$ across 16 cells (ONS76 PIEZO2 shRNA #1), $n = 25$ across 10 cells (ONS76 PIEZO2 shRNA #2), $n = 12$ across 7 cells (DAOY nt. shRNA), $n = 11$ across 8 cells (DAOY PIEZO2 shRNA #1) and $n = 15$ across 7 cells (DAOY PIEZO2 shRNA #2). Results are from four (ONS76) and three (DAOY) independent replicates. *P* value, two-sided unpaired *t*-test. Error bars, mean ± s.e.m. **d**, pMLC2 intensity on F-actin in individual ONS76 cells. $n = 64$ (static nt. shRNA), $n = 71$ (FSS nt. shRNA), $n = 47$ (static PIEZO2 shRNA #1), $n = 48$ (FSS PIEZO2 shRNA #1), $n = 76$ (static PIEZO2 shRNA #2) and $n = 81$ (FSS PIEZO2 shRNA #2) cells from three independent replicates. *P* value, two-sided unpaired *t*-test. Error bars, mean ± s.e.m. **e**, GLUT1 intensity on plasma membrane-GFP in individual ONS76 cells. $n = 36$ (static nt. shRNA), $n = 41$ (FSS nt. shRNA), $n = 22$ (static PIEZO2 shRNA #1), $n = 22$ (FSS PIEZO2 shRNA #1), $n = 25$ (static PIEZO2 shRNA #2) and $n = 29$ (FSS PIEZO2 shRNA #2) cells from three independent replicates. *P* value, two-sided unpaired *t*-test. Error bars, mean ± s.e.m. **f**, GLUT1 intensity at $n = 20$ (static vehicle, static Y-27632, FSS Y-27632) and $n = 30$ (FSS vehicle) cell–cell junctions from three independent replicates. *P* value, two-sided unpaired *t*-test. Error bars, mean ± s.e.m. **g**, The number of cell clusters per 100 cells from $n = 10$ fields of view from three independent replicates (left) and 2-NBDG level in each cell from $n = 67$ (nt. shRNA), $n = 34$ (PIEZO2 shRNA #1) and $n = 36$ (PIEZO2 shRNA #2) cells from three independent replicates (right). *P* value, two-sided unpaired *t*-test. Error bars, mean ± s.e.m. **h**, The number of cell clusters per 100 cells from $n = 20$ fields of view from three independent replicates (left) and 2-NBDG level in each cell from $n = 110$ (vehicle) and $n = 37$ (Y-27632) cells from three independent replicates (right). *P* value, two-sided unpaired *t*-test. Error bars, mean ± s.e.m.

https://doi.org/10.1038/s41551-025-01487-5

mechanosensitive ion channel that mediates light touch sensation and proprioception[74], is significantly upregulated in primary SHH MB with metastasis compared with those without (Fig. 4a), while the expression of other mechanosensitive ion channels is comparable between metastatic and non-metastatic MB (Extended Data Fig. 3). In an integrated transcriptomic dataset of tumours from 390 patients with SHH MB and 291 normal cerebellum tissue samples[75], *PIEZO2* is significantly upregulated while *PIEZO1* is significantly downregulated in SHH MB (Extended Data Fig. 2m). In human MB single-cell RNA-sequencing data[76], *PIEZO2* is expressed in the neoplastic cells of WNT, SHH, Group 3 and Group 4 MB (Extended Data Fig. 4a). We examined *PIEZO1* and *PIEZO2* expression in static or FSS-treated MB cells, and found that ONS76 cells show higher *PIEZO1* expression level than *PIEZO2*, while in DAOY cells the expression of *PIEZO1* and *PIEZO2* are comparable

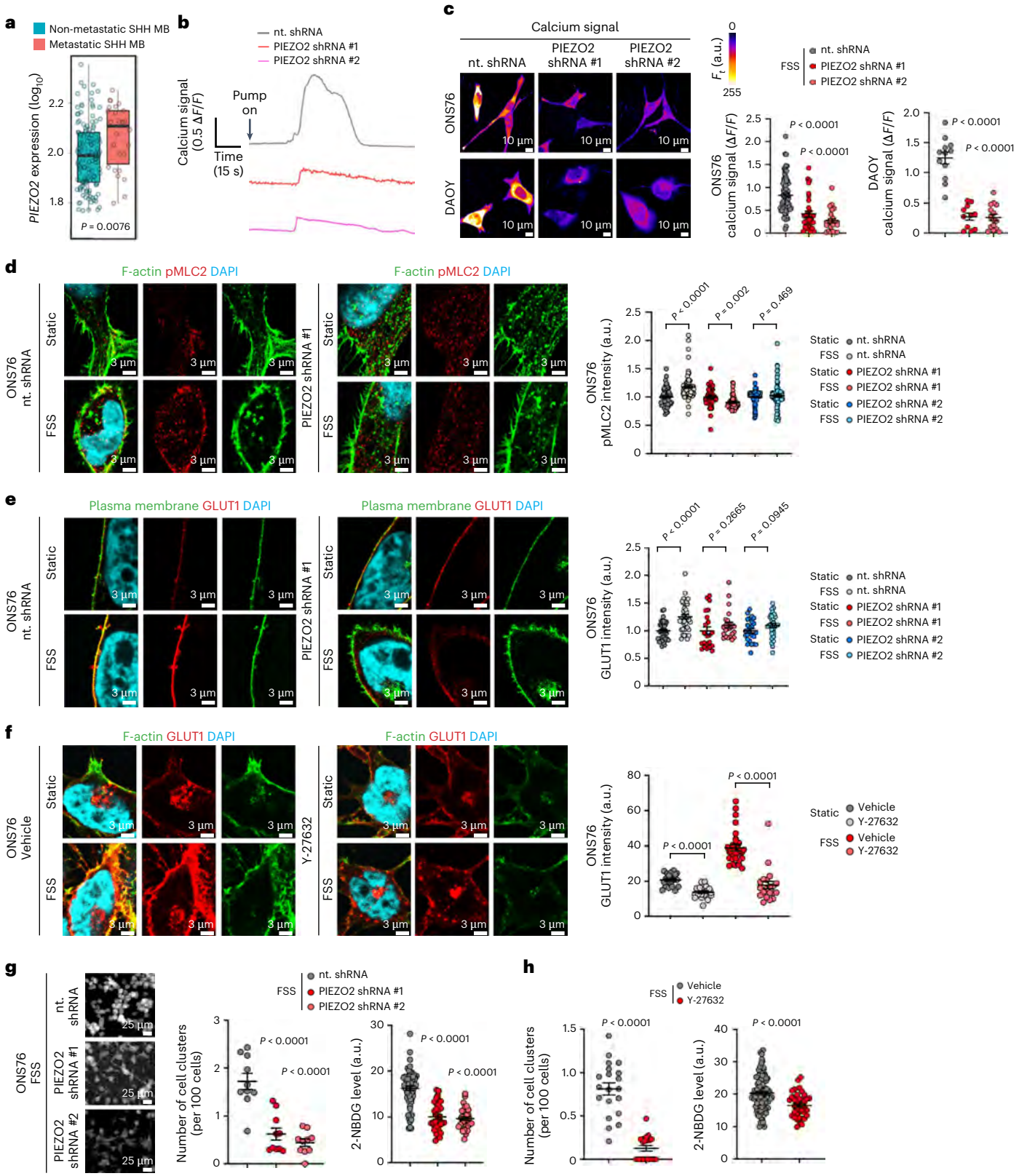

https://doi.org/10.1038/s41551-025-01487-5

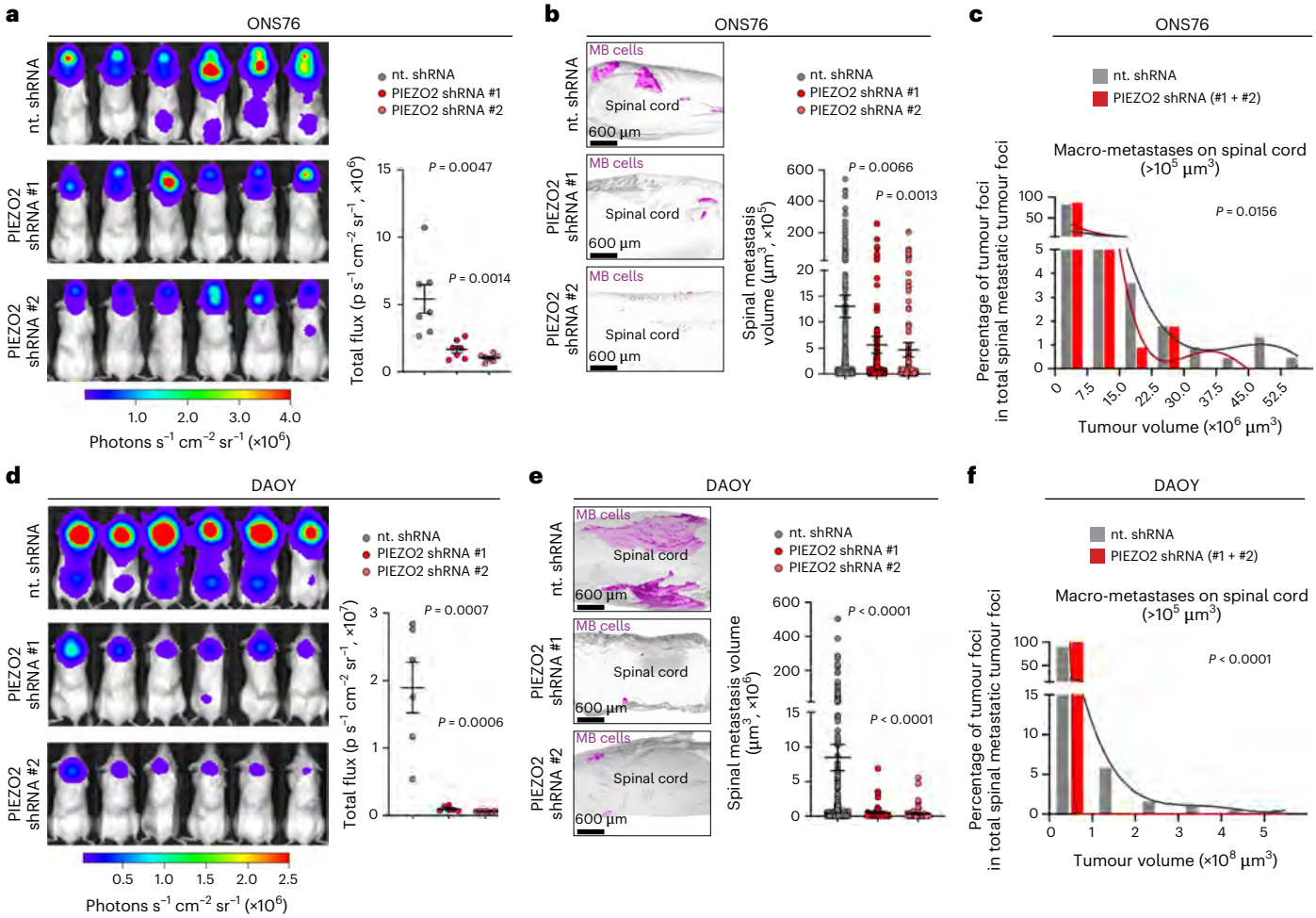

Fig. 5 | Genetic targeting of PIEZO2 mitigates MB metastasis. a, BLI shows that genetic knockdown of PIEZO2 decreases the incidence of MB metastasis in the ONS76 intracisternal xenograft model. Images were taken 24 days post implantation. The graph shows quantification of spinal radiance from $n = 7$ mice in each group. *P* values, two-sided unpaired *t*-test. Error bars, mean ± s.e.m. **b**, Fluorescence imaging of optically cleared spinal cords shows that genetic knockdown of PIEZO2 reduces the burden of metastatic MB tumours along the spinal cords in the ONS76 intracisternal xenograft model. 3D reconstructions of the spinal cords (autofluorescence) and tumours (ZsGreen) are shown. The graph shows quantifications of spinal metastasis volume of $n = 579$ (nt. shRNA), $n = 212$ (PIEZO2 shRNA #1) and $n = 187$ (PIEZO2 shRNA #2) tumours from 7 mice in each group. *P* values, two-sided Welch's *t*-test. Error bars, mean ± s.e.m. **c**, Abundance of spinal macro-metastases in the mice bearing ONS76 xenograft tumours. Histograms with nonlinear regression curves are shown. $n = 223$ (nt. shRNA) and $n = 113$ (PIEZO2 shRNA #1 + #2) macro-metastases from 7 mice in each group. *P* value, two-sided Welch's *t*-test. **d**, BLI shows that genetic knockdown of PIEZO2 decreases the incidence of MB metastasis in the DAOY intracisternal xenograft model. Images were taken 24 days post implantation. The graph shows quantification of spinal radiance from $n = 6$ mice in each group. *P* values, two-sided unpaired *t*-test. Error bars, mean ± s.e.m. **e**, Fluorescence imaging of optically cleared spinal cords shows that genetic knockdown of PIEZO2 reduces the burden of metastatic MB tumours along the spinal cords in the DAOY intracisternal xenograft model. 3D reconstructions of the spinal cords (autofluorescence) and tumours (ZsGreen) are shown. The graph shows quantifications of spinal metastasis volume of $n = 458$ (nt. shRNA), $n = 51$ (PIEZO2 shRNA #1) and $n = 77$ (PIEZO2 shRNA #2) tumours from 6 mice in each group. *P* values, two-sided Welch's *t*-test. Error bars, mean ± s.e.m. **f**, Abundance of spinal macro-metastases in the mice bearing DAOY xenograft tumours. Histograms with nonlinear regression curves are shown. $n = 188$ (nt. shRNA) and $n = 53$ (PIEZO2 shRNA #1 + #2) macro-metastases from 6 mice in each group. *P* value, two-sided Welch's *t*-test.

(Extended Data Fig. 4g). Upon FSS treatment, *PIEZO1* expression increased by 1.71-fold and *PIEZO2* expression by 3.19-fold in ONS76 cells, and *PIEZO1* expression increased by 1.24-fold and *PIEZO2* expression by 1.71-fold in DAOY cells (Extended Data Fig. 4h), indicating that *PIEZO2* expression is more responsive to FSS compared with that of *PIEZO1*. These data suggest that the calcium-permeating PIEZO2 channel may play a functional role in MB metastasis. To determine whether FSS increases intracellular calcium of MB cells, we engineered MB cells to express genetically encoded calcium sensor GCaMP6s, cultured them in microfluidic channels and performed calcium imaging with or without aCSF perfusion-generated FSS. MB cells responded to FSS with a sharp increase in intracellular calcium (Fig. 4b). Perfusion of calcium-free aCSF with calcium chelator ethylene glycol tetraacetic acid (EGTA) abrogated the calcium increase, indicating that extracellular calcium uptake resulted in FSS-induced calcium response (Extended Data Fig. 4b). Lentiviral shRNA-mediated knockdown of PIEZO2 suppressed FSS-induced calcium increase, establishing PIEZO2 as an FSS sensor in MB cells (Fig. 4b,c). In breast cancer, PIEZO2 mediates calcium influx to promote RhoA and Rho-associated coiled-coil kinases (ROCK) activity, which increases actomyosin contractility[77]. PIEZO2 knockdown abolished FSS-induced actomyosin contractility in MB cells, as indicated by the decreased intensity of phosphorylated myosin light chain 2 (pMLC2) (Fig. 4d). PIEZO2 knockdown also reduced FSS-induced GLUT1 enrichment at the plasma membrane of individual cells (Fig. 4e) or at cell–cell junctions (Extended Data Fig. 4c). This was accompanied by a reduction of FSS-induced glucose uptake and cell clustering (Fig. 4g and Extended Data Fig. 4d). To establish the functional requirement of actomyosin contractility in promoting GLUT1 localization at cell–cell

junctions, we applied Y-27632, a specific ROCK blocker upstream of pMLC2, to the FSS-treated or static control MB cells. Y-27632 treatment abrogated FSS-induced GLUT1 cell–cell junction localization, glucose uptake and cell clustering (Fig. 4f,h and Extended Data Fig. 4e,f), establishing that PIEZO2 promotes GLUT1-dependent glucose uptake through elevating actomyosin contraction. When cultured on MB-relevant stiffness (5,000 Pa)[66], PIEZO2 knockdown MB cells showed comparable growth compared with control cells (Extended Data Fig. 4i), suggesting that PIEZO2 knockdown does not affect MB cell proliferation in the absence of FSS. Taken together, these data demonstrate that PIEZO2 mediates FSS-sensing by MB cells to promote FSS-induced actomyosin contractility, which increases GLUT1 level at the plasma membrane for glucose uptake, collectively defining an FSS-activated PIEZO2-actomyosin-GLUT1 mechano-metastatic cascade.

Genetic knockdown of PIEZO2 suppresses MB metastasis

Since we discovered that PIEZO2 senses FSS in MB cells, we examined whether genetically depleting PIEZO2 suppresses MB metastasis. To this end, we performed intracisternal injection of MB cells[78], which were transduced with lentiviral PIEZO2 shRNA or non-targeting control shRNA, to determine the role of PIEZO2 in CSF-mediated metastasis. Non-invasive BLI showed that the incidence of spinal cord metastasis was reduced in the PIEZO2 knockdown xenografts compared with non-targeting control in both ONS76 (4/6 mice in the non-targeting shRNA group, 0/6 mice in the PIEZO2 shRNA #1 group and 0/6 mice in the PIEZO2 shRNA #2 group) and DAOY (6/6 mice in the non-targeting shRNA group, 1/6 mice in the PIEZO2 shRNA #1 group and 0/6 mice in the PIEZO2 shRNA #2 group) models (Fig. 5a,d). Optical clearing, light sheet imaging and 3D reconstructions of the spinal cords revealed a significant reduction in overall metastatic tumour burden and the abundance of macro-metastases in the PIEZO2 knockdown groups compared with the control groups (Fig. 5b,c,e,f). Furthermore, PIEZO2 knockdown decreased the incidence and burden of spinal metastases in D425 xenograft tumours, a model of Group 3 MB (Extended Data Fig. 5a,b). Collectively, these results establish that PIEZO2 is a therapeutic target of MB metastasis.

Pharmacological targeting of GLUT1 suppresses MB metastasis

While PIEZO2 genetic knockdown mitigates MB metastasis, no specific pharmacologic inhibitor of PIEZO2 has been discovered so far[3]. As such, we sought to determine the therapeutic targetability of the other nodes within the PIEZO2-actomyosin-GLUT1 mechano-metastatic cascade. Actomyosin is an essentiality of all cells. Therefore, actomyosin inhibitors are unlikely to possess high therapeutic value in vivo[79]. Given that FSS prominently increases GLUT1 level and its localization on the plasma membrane of MB cells, we investigated whether pharmacological inhibition of GLUT1 is an effective approach to treat MB metastasis. BAY-876 is a highly specific and potent GLUT1 antagonist with low metabolic clearance and high bioavailability in rats and dogs[80]. We validated that BAY-876 treatment reduced the intracellular level of fluorescent glucose analogue 2-NBDG in FSS-treated MB cells (Extended Data Fig. 6). Of note, while FSS-treated and static control MB cells showed comparable viability when cultured floating in aCSF, BAY-876 treatment increased the percentage of dead cells and Annexin V^+ apoptotic cells among MB cells subjected to FSS but not in the static control condition (Fig. 6a), suggesting that GLUT1 may play a critical role to promote the survival of MB cells in the circulating, nutrient-scarce CSF. Next, we performed xenografts followed by intrathecal delivery of BAY-876 to treat MB-bearing mice (Fig. 6b). Intrathecal BAY-876 administration was performed because (1) it maximizes the delivery of therapeutic agents in CSF within the spinal cord, (2) the delivered agent is locally contained within the CNS, and (3) it is a routinely performed clinical procedure. BAY-876 treatment decreased the incidence of metastatic tumours as evidenced by non-invasive BLI (4/7 mice in the vehicle group and 1/7 mice in the BAY-876 group of the ONS76 model; 5/7 mice in the vehicle group and 1/7 mice in the BAY-876 group of the DAOY model; Fig. 6c,f). Light sheet imaging of the optically cleared spinal cords demonstrated significantly reduced metastatic tumour burdens and the abundance of macro-metastases in the BAY-876 treatment group (Fig. 6d,e,g,h). These results demonstrate that pharmacological targeting of GLUT1 is a viable therapeutic strategy to treat MB metastasis.

MB 4th ventricle constriction correlates with metastasis

In patients, MB 4th ventricle infiltration is negatively correlated with survival outcomes[40]. However, it is unknown whether it is correlated with spinal metastasis. To determine whether there is a clinical correlation between 4th ventricle obstruction and spinal metastasis, we systematically inspected the MRIs of 88 patients with MB. Within these patients, 50 and 38 patients show fully and not fully obstructed 4th ventricle, respectively, defined by the absence or presence of clear 4th ventricle space in all MRIs of each patient. In patients with not fully obstructed 4th ventricle, 5 out of 38 patients (13.2%) exhibited spinal

Fig. 6 | GLUT1 inhibitor BAY-876 treatment mitigates MB metastasis. **a**, Percentage of trypan blue-positive dead cells and Annexin V^+ apoptotic cells among static or FSS-treated MB cells with vehicle or BAY-876. Trypan blue assay results are from $n = 17$ (ONS76 static), $n = 16$ (ONS76 FSS) and $n = 11$ (DAOY) wells. Both results are from three independent replicates. *P* value, two-sided unpaired *t*-test. Error bars, mean ± s.e.m. **b**, Experimental set-up for intrathecal delivery of BAY-876 to treat MB-bearing mice. **c**, BLI reveals that BAY-876 treatment decreases the incidence of MB metastasis in ONS76 intracisternal xenograft models. Images were taken 8 days post implantation. **d**, Fluorescence imaging of optically cleared spinal cords collected 8 days post implantation shows that BAY-876 treatment reduces the burden of metastatic MB tumours along the spinal cords in ONS76 intracisternal xenograft models. 3D reconstructions of the spinal cords (autofluorescence) and tumours (ZsGreen) are shown. Graphs show quantification of spinal metastasis volume of $n = 331$ (vehicle) and $n = 217$ (BAY-876) metastatic tumours from 7 mice in each group. *P* values, two-sided Welch's *t*-test. Error bars, mean ± s.e.m. **e**, Abundance of spinal macro-metastases in the ONS76 xenograft tumour-bearing mice treated with vehicle or BAY-876. Histograms with nonlinear regression curves are shown. $n = 95$ (vehicle) and $n = 42$ (BAY-876) macro-metastases from 7 mice in each group. *P* value, two-sided Welch's *t*-test. **f**, BLI reveals that BAY-876 treatment decreases the incidence of MB metastasis in DAOY intracisternal xenograft models. Images were taken 8 days post implantation. **g**, Fluorescence imaging of optically cleared spinal cords collected 10 days post implantation shows that BAY-876 treatment reduces the burden of metastatic MB tumours along the spinal cords in DAOY intracisternal xenograft models. 3D reconstructions of the spinal cords (autofluorescence) and tumours (ZsGreen) are shown. Graphs show quantification of spinal metastasis volume of $n = 357$ (vehicle) and $n = 117$ (BAY-876) metastatic tumours from 4 (vehicle) and 5 (BAY-876) mice. *P* values, two-sided Welch's *t*-test. Error bars, mean ± s.e.m. **h**, Abundance of spinal macro-metastases in the DAOY xenograft tumour-bearing mice treated with vehicle or BAY-876. Histograms with nonlinear regression curves are shown. $n = 169$ (vehicle) and $n = 35$ (BAY-876) macro-metastases from 4 (vehicle) and 5 (BAY-876) mice. *P* value, two-sided Welch's *t*-test. **i**, Patients with MB with fully obstructed 4th ventricle show increased rates of spinal metastasis compared with patients with not fully obstructed 4th ventricle. Patients were defined as having fully obstructed 4th ventricle if clear 4th ventricle space was absent throughout all brain MRIs of that patient. $n = 38$ (not fully obstructed) and $n = 50$ (fully obstructed). *P* value, one-sided chi-square test. **j**, FSS activates a targetable mechano-metastatic cascade to promote MB metastasis. Left: primary MB tumour growth obstructs the 4th ventricle, leading to increased FSS. PIEZO2 perceives FSS to permeate calcium into tumour cells. Elevated intracellular calcium promotes actomyosin contractility, which drives the recruitment of GLUT1 to plasma membrane for glucose uptake. We propose that FSS-induced MB cell clustering is mediated by the E-cadherin and β-catenin complex that physically binds F-actin. Right: the FSS–PIEZO2–actomyosin–GLUT1 axis comprises the mechano-metastatic cascade. Key nodes in the cascade, including PIEZO2, actomyosin and GLUT1, are vulnerabilities to mitigate MB metastasis. Schematic in **b** and model diagram in **j** were created using BioRender.com.

https://doi.org/10.1038/s41551-025-01487-5

metastasis, while in patients with fully obstructed 4th ventricle, 30 out of 50 patients (60%) exhibited spinal metastasis (Fig. 6i), suggesting that MB 4th ventricle obstruction is significantly correlated with spinal metastasis. These findings further support that FSS promotes MB metastasis in vivo.

Discussion

Cellular processes, such as cell–biofluid interaction, cell–cell interaction and cell–ECM interaction, generate FSS, compressive stress and tensile stress that are spatiotemporally dynamic[3,22,61]. FSS is a ubiquitous mechanical stimulus that regulates functional states of cells. Force-sensitive cation channels PIEZOs sense FSS to orchestrate diverse developmental and homeostatic processes: PIEZO1 senses FSS to regulate vasculature formation, blood pressure regulation[81–83], lymphatic development[84] and renal function[85]. PIEZO2 is the primary mechanosensor that mediates vital sensory functions such as touch and pain[86,87] and proprioception[88]. PIEZO2 senses FSS to regulate endothelium integrity in lung microvasculature[89], lung inflation[90] and urination[91]. While a growing body of evidence reveals that PIEZO-dependent FSS sensing regulates the functional states of cells, how FSS is influenced by the expanding brain tumour mass, which, in turn, governs tumour cell behaviours to dictate metastatic success, remained completely

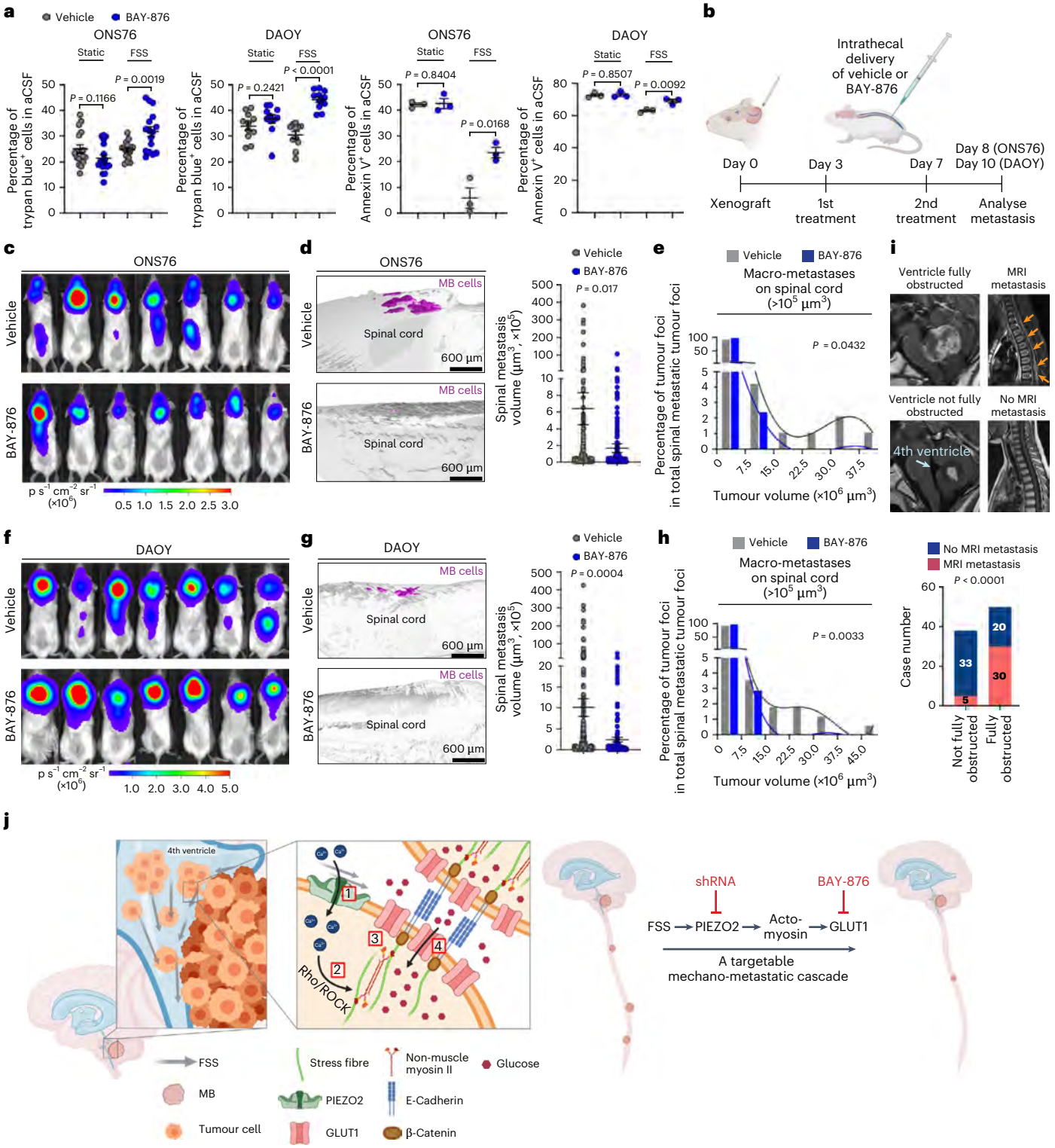

unknown. Here we define a mechano-metastatic cascade driven by PIEZO2 that promotes MB metastasis (Fig. 6j): MB tumour growth at the 4th ventricle physically obstructs the CSF conduit, most prominently at the cervicomedullary junction, which elevates FSS at the CSF–tumour interface. Heightened FSS induces an amoeboid-like cell state with behaviours conducive to metastasis, including elevated cell motility, increased ECM degradation and weakened cell-substrate adhesion. PIEZO2 perceives FSS to increase intracellular calcium. This promotes plasma membrane enrichment of GLUT1 and glucose uptake in an actomyosin contractility-dependent manner. Genetic knockdown of PIEZO2 or inhibiting GLUT1 function using BAY-876 robustly mitigates MB metastasis. We thereby unveil novel therapeutic vulnerabilities of metastatic MB.

We used computational fluid dynamics to simulate CSF flow with varying degrees of conduit obstruction by brain tumour. Time-lapse MRI has revealed CSF flow, brain motion and deformability in human subjects, enabling CSF flow modelling within the entire CNS with dynamic boundary conditions[92–97]. However, precise measurements of these parameters in brain tumour patients are lacking. Future studies are warranted to determine how brain tumour growth affects compliance and deformability of the CSF conduit to model more accurate and individualized CSF flow parameters. In normal conditions, the CSF is a Newtonian fluid with comparable viscosity and density to water[98,99]. However, brain tumour patients exhibit elevated circulating nucleic acids, proteins and cells in the CSF[100]. Elevated protein and cell concentrations in the CSF were shown to confer weakly non-Newtonian behaviour[101]. These properties would affect the calculated FSS values in the microchannels and on the orbital shaker[102]. Therefore, determining the rheological properties of the CSF in brain tumour patients would enable more precise modelling of CSF flow dynamics within microfluidic channels and the orbital shaker.

Recently, we reported that MB cells ensheathe tumour blood vessels to construct the blood–tumour barrier in the primary tumour. These cells are mechanosensitive in a Piezo2-dependent manner. Genetic knockout of Piezo2 increases blood–tumour barrier permeability and the chemosensitivity of MB[20]. Together with findings reported here, we propose that targeting PIEZO2 is a two-in-one strategy to increase primary MB chemosensitivity and decrease MB metastasis. While dietary intervention of PIEZO2 function using omega-3 fatty acid eicosapentaenoic acid was reported[103], this approach has low potency and specificity. Currently, there are no specific and potent pharmacological modulators for PIEZO2[74]. Our discoveries not only underscore the need to develop PIEZO2-modulating chemical agents but also highlight the potential of targeting PIEZO2-activated downstream signalling mechanism to circumvent the lack of the PIEZO2 antagonist.

Cancer cells perform aerobic glycolysis (the Warburg effect) to fuel energy-intensive processes such as proliferation, migration and survival under stress[104]. This increase in glucose demand can be met by overexpression of GLUT1 and GLUT3[105]. Given that GLUT3 is expressed in neurons and is required for neuronal glucose uptake[106], inhibiting GLUT1 is an attractive tumour-agnostic therapeutic strategy to target cancer cells while reducing neurotoxicity. Several GLUT1 inhibitors, including BAY-876[80], WZB-117[107] and STF-31[108], have been developed that demonstrated preclinical antineoplastic efficacy. BAY-876 has low metabolic clearance and high oral bioavailability in rats and dogs[80], showing potential as a candidate for clinical development. Given that BAY-876 exhibits in vivo efficacy against metastatic MB as demonstrated by our study, further investigation is warranted to determine the optimal administration route, therapeutic index and toxicity profile for clinical use.

Multiple human malignancies, such as lung, breast, skin and haematological cancer, metastasize to the CNS leptomeninges. Patients with leptomeningeal metastasis have an overall survival of 4–6 months[109]. Determining how disseminated cancer cells survive in the nutrient-scarce CSF may reveal molecular vulnerabilities for targeted therapies. Breast and lung cancer cells in the CSF secrete complement component 3, which remodels the blood–CSF barrier to promote leakage of plasma nutrients into the CSF[110]. Iron uptake through lipocalin-2 promotes cancer cell survival in the CSF and drives leptomeningeal metastasis[111]. Here we show that glucose uptake through GLUT1 mediates leptomeningeal metastasis of MB. Given that the CSF contains approximately two-thirds of the glucose that is present in the blood[64], and multiple cancer types rely on glucose for energy[104], our findings provide impetus for investigating whether GLUT1-mediated glucose uptake is a tumour-agnostic mechanism for cancer cell survival in the CSF.

In patients, MB metastases are present along the brain–spinal cord axis, unresectable and refractory to chemotherapy and irradiation, making metastatic MB universally high risk[30]. Owing to the complex mechanical cues that MB cells experience in primary tumour, within CSF or blood[23], or at distant sites during metastatic outgrowth, PIEZO2 may be an essential but not the only mechanosensor that dictates metastatic success. FSS activates PIEZO1 to sensitize tumour cells to tumour necrosis factor-related apoptosis-inducing ligand (TRAIL)-mediated apoptosis in glioblastoma[112] and prostate cancer cells[113]. Several cell-based and nanoparticle-based methods to effectively deliver TRAIL to circulating tumour cells have been developed[114–120]. While MB cells do not appear to express PIEZO1 in vivo[20], whether activation of PIEZO2 or other mechanosensors sensitizes MB cells to TRAIL-mediated apoptosis warrants future studies. Furthermore, systematically determining the microenvironmental mechanical cues and defining the mechanosensors during various phases of metastasis should reveal further therapeutic opportunities to tackle this lethal phase of the disease. MB transcriptionally mirrors neurodevelopment[121–123] and its metastasis is driven by co-option of a neurodevelopmental epigenetic programme[124]. Our report of the functional importance of PIEZO2 in MB raises the intriguing question of whether PIEZO2 regulates normal cerebellum development. Indeed, cell proliferation, migration and cerebellar folding[125] may provide ample mechanical stimuli to modulate the activity of PIEZO2 or other mechanosensitive molecular machineries.

Methods

Cell culture

Human MB cell lines ONS76[126], DAOY and D425[127] were a gift from M. Taylor. DAOY and ONS76 cells were cultured using DMEM with 10% FBS. D425 cells were cultured using 50:50 neural basal medium and DMEM/F12 supplemented with non-essential amino acids, sodium pyruvate, HEPES, glutamine, B27, heparin, 25 ng ml^{-1} human leukaemia inhibitory factor, 25 ng ml^{-1} bFGF and 25 ng ml^{-1} human EGF without addition of serum. For aCSF medium, cells were cultured in 125 mM NaCl, 2.5 mM KCl, 26 mM $NaHCO_3$, 1.25 mM NaH_2PO_4, 2 mM $CaCl_2$, 1.2 mM $MgCl_2$, 15 mM glucose, 2% DMEM, 0.2% FBS and 100 U ml^{-1} penicillin–streptomycin.

All cell lines were regularly checked for mycoplasma infections and treated with Plasmocin (Invivogen #ant-mpt-1) when infection was noted. No cell line is listed in the database of commonly misidentified cell lines maintained by the International Cell Line Authentication Committee and National Center for Biotechnology Information BioSample.

Lentiviral transduction

For PIEZO2 knockdown, pLKO.1 lentiviral shRNA target gene set and pLKO.1-TRC-control vector were acquired from Dharmacon. The mature antisense sequences were shRNA #1 (TAATTGTAGCTCTTGGTGAGG) and shRNA #2 (TTTCAACTGGCTTTGTTGGGC). For membrane GFP tagging, MB cells were transduced with the FUmGW (Addgene #22479) construct. For expression of firefly luciferase and ZsGreen for xenografts, MB cells were transduced with the pHIV-Luc-ZsGreen (Addgene #39196) construct. For calcium imaging, MB cells were transduced with the GCaMP6s-TdTomato construct (Addgene #80316). For all cells transduced with a fluorescence-expressing construct, transduced cells were purified using fluorescence-activated cell sorting.

Microfluidic channel fabrication and culture

The microfluidic channel consisted of one polydimethylsiloxane (PDMS) layer and a glass slide on which the PDMS layer was bonded. The channel within the PDMS layer was 120 µm high and 2 mm wide. The microfluidic device was fabricated through multilayer soft lithography. First, SU-8 2075 photoresist (Microchem) with a thickness of 120 µm was spin-coated onto a silicon wafer and then patterned into the SU-8 mould of the PDMS layer by standard photolithography. After that, a precursor mixture of PDMS base and cross-linker (Sylgard 184, Dow Corning) at the w/w ratio of 10:1 was poured onto the SU-8 mould and cured at 80 °C for 45 min. Finally, the PDMS layer was peeled from the SU-8 moulds, punched with open inlet and outlet holes, and bonded to the glass slide.

The microfluidic channels were sterilized by soaking in 70% ethanol overnight. The devices were washed with phosphate-buffered saline (PBS) and coated with 0.02 mg ml^{-1} poly-L-lysine (Sigma, P2636) or 1 µg ml^{-1} RGD peptide (Cell Guidance Systems, AP16) in PBS for 2 h at room temperature. DAOY and ONS76 cells were seeded into microfluidic channels at a density of 1,000,000 cells per ml in aCSF.

For PDMS channel dimensions measurement, channels were loaded with Alexa Fluor 555-Cadaverine (Thermo Fisher Scientific, A30677) diluted 1:500 in PBS. A spinning disk confocal microscope (Quorum) was used with 10×/0.4 numerical aperture (NA) objective to obtain Z-stacks of the Alexa Fluor 555 signal. The width and height of channels were measured using ImageJ (version 1.54d) before and after overnight 70% ethanol soaking.

FSS application

One day after seeding, aCSF flow was applied to cells cultured in microfluidic channels using a programmable syringe pump (Harvard Apparatus) through a polytetrafluoroethylene tubing. Microfluidic shear stress (τ) within the channel was calculated using the following equation: $\tau = 6\eta Q/h^2 w$, where η represents the viscosity of the medium, Q flow rate, h height and w width of the channel[128]. With approximate viscosity of aCSF medium at 37 °C of 1cP, 15 µl min^{-1} flow rate and 2,000 µm by 120 µm channel dimensions, the τ is 0.52 dyne cm^{-2}.

For orbital shaking, VWR Mini Shaker (VWR #12620-938) was placed in a tissue culture incubator. MB cells cultured on 6-well plates in aCSF were placed on the orbital shaker and gyrated at 100 rpm for 18 h. The fluid flow profile and FSS were determined using numerical simulation.

Numerical simulation of the orbital shaker well and calculation of the shear forces

A model well of 35 mm in diameter and 10 mm in depth filled with water (1.8 mm in depth) was simulated with 100 rpm with a gyration of 3 mm. COMSOL Multiphysics was used to simulate the rotation of the well. The computational domain was designed with the lower part of the cylinder filled with water and the upper part occupied by air initially. The dynamic viscosity and density of water at room temperature were applied. The working parameters of the simulation were as follows: well diameter D = 35 mm, liquid height in well H_{water} = 1.8 mm, depth of well H_{well} = 10 mm, orbital rate ω = 100 rpm, gyration diameter d = 3 mm, radius r = 1.5 mm, viscosity of water μ_w = 0.001 Pa s, density of water ρ_w = 1,000 kg m^{-3}, viscosity of air μ_a = 18.49 µPa s and density of air ρ_a = 1.184 kg m^{-3}. Owing to the low Reynolds number of the set-up, laminar flow module, including the continuity equation and Navier–Stokes equation, and moving mesh were applied to calculate the flow field and to determine the water–air interface, as shown below:

$$\rho_i [\boldsymbol{u}_i \times \nabla \boldsymbol{u}_i] = -\nabla P + \mu_i \nabla^2 \boldsymbol{u}_i - \rho_i \mathbf{g} \quad (1)$$

$$\nabla \boldsymbol{u}_i = 0 \quad (2)$$

where ρ_i, $\boldsymbol{u}_i$ and μ_i are the density, velocity and dynamic viscosity of the fluid (i = water or air), $\mathbf{g}$ is the gravitational acceleration and P is the pressure. A moving boundary condition was applied on the well surfaces. The function of the moving boundary condition is as follows:

$$\begin{cases} u_x = 2\pi\omega r \times \sin(2\pi\omega t) \\ u_y = 2\pi\omega r \times \cos(2\pi\omega t) \\ u_z = 0 \end{cases} \quad (3)$$

A meshing independent study was conducted and 24,855 meshing elements were applied during the finite element analysis. A time-dependent study of a 2 s period of rotation was studied and the motion of the water–air interface with velocity field was extracted. The shear stress (τ_s) on the well substrate owing to the rotation of fluid was calculated by equation (4):

$$\tau_s = \delta_{sr} \times \mu_w \quad (4)$$

where δ_{sr} is the shear rate of water at the substrate surface and μ_w is the dynamic viscosity of water. Supplementary Video 1 shows the distribution of shear stress subjected to the substrate, where the average shear stress is ~0.17 dyne cm^{-2} and a maximum FSS of ~0.40 dyne cm^{-2} appears at the periphery of the substrate.

Live imaging

For live imaging, MB cells were seeded in microfluidic channels and cultured in aCSF. The channels were placed in an environmental chamber maintaining 37 °C and 5% CO_2 equipped on an epifluorescence microscope (Nikon). Bright-field images were acquired using 10×/0.5 NA or 20×/0.75 NA object at 1 frame per minute. ImageJ (version 1.54d) Manual Tracking plugin was used to generate cell movement coordinates. The coordinates were plugged into the Chemotaxis and Migration Tool (Ibidi) to generate cell maps and motility quantifications.

Calcium imaging

ONS76 and DAOY cells expressing GCaMP6s-TdTomato (Addgene #80316) were cultured in microfluidic channels in aCSF. For PIEZO2 knockdown studies, cells were transduced with non-targeting (nt.) or PIEZO2 shRNAs 3.5 days before calcium imaging. Immediately following removal from the incubator, GCaMP6s signal from the MB cells was imaged using a 491 nm laser at 2 frames per second with aCSF flow from a syringe pump (Harvard Apparatus). For extracellular calcium-free experiments, aCSF without calcium with 0.5 mM EGTA was perfused. Live imaging was performed on a spinning disk confocal microscope (Quorum) with 40×/1.1 NA objective and Volocity (Quorum, version 6.3.1). Cells with comparable tdTomato expression across experimental groups and replicates were chosen for imaging. Active calcium compartments within the MB cells were identified as previously described[129]. In brief, upon FSS application, subcellular calcium compartments where initial spike and subsequent flashing occurred were identified. GCaMP6s fluorescence intensity within each compartment was quantified and analysed using ImageJ (version 1.54d) and Excel (Microsoft, version 2405). The calcium signal was calculated by the following equation: $\Delta F/F_0 = (F_t - F_0)/F_0$, where F_t is the GCaMP6s intensity at time t and F_0 is the baseline GCaMP6s intensity before aCSF flow application.

Glucose uptake assay

Glucose uptake was measured using the Glucose Uptake Cell-Based Assay Kit (Caymen Chemical 600470), which utilizes the fluorescent glucose analogue 2-NBDG. MB cells were grown to confluency on poly-L-ornithine (PLO; Sigma-Aldrich #A-004-C) and laminin (1:200 in PBS, Sigma-Aldrich #L2020)-coated 6-well plates. Cells were then incubated with aCSF without glucose for 30 min and then supplied with aCSF containing 33.3 µg ml^{-1} 2-NBDG. After 18 h of orbital shaking or static culture, cells were washed with the Cell-Based Assay Buffer and then live-imaged using a spinning disk confocal microscope with Volocity (Quorum, version 6.3.1). A 10×/0.4 NA objective was used with a 491 nm laser to image 2-NBDG fluorescence. The sample holder

was equipped with an environmental chamber that maintained 37 °C and 5% CO_2.

For Y-27632 treatment, MB cells were pre-incubated in aCSF with 10 μM Y-27632 (Tocris #1254) or equivalent volume of DMSO (0.1%) for 30 min and treated with Y-27632 or DMSO throughout orbital shaking or static culture. For the BAY-876 experiment, MB cells were treated with 1 μM BAY-876 (Tocris #6199) or equivalent volume of DMSO (0.05%) overnight and throughout orbital shaking or static culture for a total of 2 days. For *PIEZO2* knockdown, MB cells were transduced with lentiviral shRNA upon seeding onto PLO and laminin-coated 6-well plates. Two days later, 2-NBDG treatment and orbital shaking were performed. 2-NBDG fluorescence intensity quantification was performed using ImageJ (version 1.54d). Cell clusters were identified as five or more cells in contact with one another.

Cell death and flow cytometry assays

For BAY-876 treatment, MB cells were seeded onto low-adhesion 6-well plates (Corning #3471) at a density of 2,500,000 cells per well in aCSF containing 1 μM BAY-876 or equivalent volume (0.1%) DMSO. After 18 h of orbital shaking or static culture, trypan blue dead cell counting assay or Annexin V/PI flow cytometry was performed. For cell counting, the percentage of trypan blue-positive dead cells was measured using the automated Vi-Cell XR Cell Viability Analyzer (Beckman Coulter). For Annexin V/PI flow cytometry, Alexa Fluor 488 Annexin V for the flow cytometry kit (Invitrogen #V13241) was used according to the manufacturer's protocols, and flow cytometry was performed using Fortessa UVBGR (Fortessa). The percentage of Annexin V-positive cells was quantified using FCS Express 7 (De Novo Software).

For measurement of floating to adherent cell ratio, MB cells were seeded onto PLO and laminin-coated 6-well plates at a density of 200,000 cells per well. After 2 days, the medium was replaced with aCSF and cells were cultured under orbital shaking or static condition. At the indicated time points, the supernatant was collected for floating cells, and trypsinization was performed for adherent cells. Trypan blue-negative live cell count was measured using the Vi-Cell platform, and the ratio of the number of cells in the supernatant to the adherent fraction was calculated.

Microfluidic adhesion assay

Adhesion assay was performed as previously described[51,52]. In brief, MB cells were cultured with aCSF in microfluidic channels. Following 6 h of 15 μl min^{-1} aCSF flow treatment or static culture, the microfluidic channels were placed on a sample holder attached to an epifluorescence microscope (Nikon). A linear gradient of aCSF flow (0–10.8 ml min^{-1}) was applied to the cells using a programmable syringe pump (Harvard Apparatus), while time-lapse imaging was performed at 15 s per frame, so that the FSS at each time point could be calculated. Cells detach at the point where FSS exceeds the cell-substrate adhesion strength. The number of cells at each frame was quantified using ImageJ (version 1.54d), and the percentage of shed cells was plotted using Prism (GraphPad, version 10.0.3). The syringe capacity of the pump enabled a gradient flow with 375 dyne cm^{-2} as the maximum FSS. Since more than half of the static control cells on the PLL substrate remained attached after the gradient flow, τ_{50} (FSS at which 50% of cells detach) could not be calculated. Therefore, τ_{75} (FSS at which 25% of cells detach) was calculated as previously described[53–55]. In brief, the percentage of cells attached was plotted against FSS, nonlinear regression curve was fitted, and τ_{75} was interpolated.

Polyacrylamide stiffness gel preparation

Polyacrylamide gels with 500 Pa and 5,000 Pa stiffness were fabricated on glass coverslips as previously described[16,20]. Polyacrylamide gel solutions were prepared by mixing acrylamide (5%, Bio Basic #AB1032) and bis-acrylamide (0.011% for 500 Pa, 0.14% for 5,000 Pa, BioShop #ACR007) in HEPES buffer. Polymerization was initiated with 0.05% ammonium persulfate (Sigma) and 0.1% *N*,*N*,*N*′,*N*′-tetramethylethylenediamine (Sigma). Each solution (15 μl) was pipetted onto glass coverslips treated with 0.5% 3-aminopropyltrimethoxysilane (Sigma) and 1% glutaraldehyde (Sigma). To cross-link ECM protein onto the polyacrylamide gel surface, the gels were photoactivated by Sulfo-SANPAH (Sigma) under ultraviolet light for 8 min. Subsequently, gels were sterilized with peracetic acid for 10 min, washed and then incubated in 200 μg ml^{-1} laminin solution (Sigma) at 37 °C overnight.

For GLUT1 immunostaining, 20,000 ONS76 cells were seeded onto 500 Pa or 5,000 Pa stiffness gels in 12-well plates, grown for 2 days in DMEM + 10% FBS medium, 1 day in aCSF, and then fixed with paraformaldehyde (PFA) at room temperature for 20 min followed by immunostaining. For cell counting, 5,000 ONS76 cells treated with nt. or PIEZO2 shRNA were seeded onto 5,000 Pa stiffness gels. From day 2 to day 6, images were acquired every 2 days using a Nikon DS-L3 camera connected to a Nikon Eclipse TS100 inverted microscope with 10× objective. Cell numbers were quantified in three randomly selected fields of view per replicate in three replicates and then extrapolated to the area of the coverslip.

Immunofluorescence staining

For experiments involving microfluidic channels, cells were stained directly within the devices. For orbital shaker experiments, cells were grown on 35 mm glass-bottom dishes (Ibidi #81158) coated with PLO and laminin. For *PIEZO2* knockdown experiments, staining was performed 3.5 days after lentiviral shRNA transduction. For Y-27632 treatment experiments, cells were pre-incubated with 10 μM Y-27632 or equivalent volume DMSO (0.1%) for 30 min in aCSF and then treated for a further 18 h throughout orbital shaking. To perform immunofluorescence staining, cells were fixed with 4% PFA at 4 °C overnight and then washed with PBS containing 0.1% Triton X-100 (Bio Basic #TB0198) (PBST). Cells were blocked with 10% normal goat serum (NGS; Sigma-Aldrich #G9023) in PBST for 1 h, and then incubated with primary antibody overnight at 4 °C and secondary antibody for 1 h at room temperature. For F-actin staining, cells were incubated with phalloidin (1:200, Invitrogen #A12379) in PBS for 20 min at room temperature. Immunofluorescence of GLUT1 in MB patient biopsies was approved by Xiangya Hospital Ethics Committee (#2025010216). The primary antibodies used were STEM121 (1:50; Takara #Y40420), rabbit anti-ColIV (1:100; BioRad #2150-1470), rabbit anti-GLUT1 (1:200; Sigma-Aldrich #07-1401), rabbit anti-phospho-myosin light chain 2 (1:100; Cell Signaling Technology #3671S), mouse anti-phospho-myosin light chain 2 (1:100; Cell Signaling Technology #3675S), rabbit anti-phospho-FAK (Tyr397) (1:100; Invitrogen #44-625G) and rabbit anti-caveolin-1 (1:100; Cell Signaling Technology #3267). The secondary antibodies used were Alexa Fluor 488 donkey anti-mouse IgG (1:200–400; Jackson Immunoresearch #715-545-151), Alexa Fluor 594 donkey anti-rabbit IgG (1:200–400; Jackson Immunoresearch #711-585-152), Alexa Fluor 647 donkey anti-mouse IgG (1:200–400; Jackson Immunoresearch #715-606-151) and Alexa Fluor 647 donkey anti-rabbit IgG (1:200–400; Jackson Immunoresearch #711-605-152). Primary antibodies were diluted in blocking solution, and secondary antibody was diluted in blocking solution containing 1 μg ml^{-1} DAPI. Images were acquired using a spinning disk confocal microscope (Quorum) with 10×/0.4 NA, 40×/1.3 NA or 63×/1.4 NA objective and Volocity (Quorum, version 6.3.1). Quantifications were performed using Volocity (Quorum, version 6.3.1), ImageJ (version 1.54d) and Imaris (Oxford Instruments, version 10.1.1). For pMLC2 intensity and GLUT1 localization to plasma membrane of nt. or PIEZO2 shRNA-treated cells (Fig. 4d,e), intensity values were normalized to the respective static control for each shRNA treatment group.

ECM degradation assay

Oregon Green-tagged gelatin (Invitrogen #G13186) was dissolved in PBS with 2% sucrose to a concentration of 1 mg ml^{-1}. Glass-bottom dishes (35 mm) were coated with PLO for 20 min and then with Oregon

Green-gelatin for 1 h at room temperature. Coated dishes were washed with PBS and seeded with 200,000 MB cells. After 2 days, the medium was replaced with aCSF and 18 h of orbital shaking or static culture was performed. Cells were then fixed with 4% PFA at room temperature for 15 min. Oregon Green-gelatin signal was imaged using a spinning disk confocal microscope (Quorum) with 63×/1.4 NA objective and Volocity (Quorum, version 6.3.1). Quantification of degraded Oregon Green-gelatin patches was performed using ImageJ (version 1.54d).

RT-qPCR

RNA from static or orbital shaker-treated MB cells cultured in aCSF were collected using the RNeasy Plus Mini Kit (Qiagen, #74134). Reverse transcription was performed using the SensiFAST cDNA Synthesis Kit (Bioline, #BIO-65054). qPCR was performed using the PowerUp SYBR Green Master Mix (Applied Biosystems, #A25742) using the following primers: human PIEZO1 forward, TTCCTGCTGTACCAGTACCT; human PIEZO1 reverse, AGGTACAGCCACTTGATGAG; human PIEZO2 forward, CACCTGGCTACAACTGCTCA; human PIEZO2 reverse, CCCGATGTCAGGTACAAACA; human PSGL1 forward, AGAAGCCACTTCTTCTGGGC; human PSGL1 reverse, CAGAGGCATGGCACCACC; human ESL1 forward, ACCGAGGCAACATCACTGAG; human ESL1 reverse, GCATCCTTTTCTCCAAGCCG; human CD44 forward, CCAGAAGGAACAGTGGTTTGGC; human CD44 reverse, ACTGTCCTCTGGGCTTGGTGTT.

RNA-seq

RNA was collected from static control or orbital shaker-treated ONS76 and DAOY cells cultured in aCSF. Total RNA was collected after 18 h of treatment using the RNeasy Plus Mini Kit (Qiagen, #74134). RNA integrity number (RIN) was determined using the Agilent Bioanalyzer. All samples had RIN >9.8. Library preparation was performed using the NEBNext Ultra II Directional polyA mRNA Library Prep Kit. Sequencing was performed on Illumina NovaSeq with 30 million paired-end reads per sample at 100 bp read length.

Processing of bulk RNA-seq data of cultured cells

Paired-end RNA-seq data of ONS76 and DAOY were aligned to GRCh38 using Hisat2 (v 2.2.1)[130]. Quantification of aligned bam at the gene level was performed with the featureCounts function in R package Rsubread (v 2.18.0)[131]. Differential expression analysis was performed using R package DESeq2 (v 1.44.0)[132]. DEGs were filtered with the following parameter: |Log2FoldChange| > 0.75, adjusted *P* value < 0.05. Clustering of DEGs was performed with R package clusterProfiler (v 4.12.0)[133]; the results were filtered with the following parameter: *q*-value < 0.05. All DEGs were then visualized with R package ComplexHeatmap (v 2.20.0)[134]. The raw data were deposited to Gene Expression Omnibus (GEO) under accession number GSE288458 (ref. 135).

Mouse experiments

Female NOD SCID gamma /J#5557 immunodeficient mice aged 8–12 weeks were used for this study. Mice were housed under aseptic conditions with filtered air and sterilized food, water, bedding and cages under a 12 h/12 h light/dark cycle, 21–23 °C and 40–60% humidity at The Centre for Phenogenomics (TCP) in Toronto, Canada. Animal procedures followed the Animals for Research Act of Ontario and the Guidelines of the Canadian Council on Animal Care, as approved by the TCP Animal Care Committee (protocol 27-0288H).

For orthotopic xenografts, mice were anaesthetized using gaseous isoflurane and immobilized in a stereotaxic head frame. The skull of the mouse was exposed, and a small opening was made using a sterile dental drill (Precision Guide) at 2 mm posterior to lambda and 2 mm deep. At this location, Luc-ZsGreen-expressing ONS76 or DAOY cells in 2 µl culture media were injected at a rate of 1 µl min^{-1} using a programmable syringe pump (Harvard Apparatus) and a 30-gauge Hamilton syringe.

For intracisternal xenografts, mice were anaesthetized using gaseous isoflurane, and the head was bent in a stereotaxic frame by approximately 90°. The skin and muscle layers above the atlanto-occipital membrane were cut to expose the cisterna magna. Luc-ZsGreen-expressing MB cells suspended in 5–8 µl sterile ice-cold PBS were injected as previously described[136] using a 30-gauge Hamilton syringe. All procedures were performed under sterile conditions.

For all xenograft experiments, BLI was performed using the Xenogen IVIS Lumina System coupled to LivingImage software (PerkinElmer, version 4.7.0) for data acquisition. Mice were anaesthetized using gaseous isoflurane and imaged 10 min after intraperitoneal injection of 100 mg kg^{-1} luciferin.

For orthotopic xenograft of FSS-treated cells, MB cells (ONS76 and DAOY) were seeded onto PLO and laminin-coated 6-well plates. Two days post seeding, the medium was changed to aCSF and cells were subjected to orbital shaking (VWR) at 100 rpm for 18 h. The number of cells injected was 2,000 for both ONS76 and DAOY. BLI was performed every 7 days.

For PIEZO2 knockdown intracisternal xenografts, MB cells (ONS76, DAOY and D425) were transduced with lentiviral shRNA targeting PIEZO2 or non-targeting controls at approximately 0.7 multiplicity of infection for 24 h. For ONS76 and DAOY, cells were seeded onto PLO and laminin-coated 6-well plates, and for D425, cells were cultured in suspension. Two days post transduction, the medium was changed to aCSF, and cells were subjected to orbital shaking (VWR) at 100 rpm for 18 h. The number of cells injected was 450,000 for ONS76 and DAOY, and 225,000 for D425. BLI was performed at day 7 and every subsequent 3 days. Total spinal BLI radiance was quantified using LivingImage software (PerkinElmer, version 4.7.0). For the BAY-876 treatment experiment, MB cells (ONS76 and DAOY) seeded in PLO and laminin-coated 6-well plates were cultured in aCSF and treated with 18 h of orbital shaking at 100 rpm. The number of cells injected was 600,000 for ONS76 and 300,000 for DAOY. BLI was performed 2 days after xenograft. Mice were then assigned to the DMSO or BAY-876 groups in a BLI signal-balanced manner. For intrathecal injections, BAY-876 (MedChemExpress, HY-100017) was prepared in 5% DMSO, 10% NMP and 85% PEG300. BAY-876 (3.84 mg kg^{-1}) or solvent control was intrathecally injected using a 26-gauge Hamilton syringe through the L5-6 lumbar spine at day 3 and day 7 post xenograft.

For immunohistochemistry, xenograft mice were euthanized by intracardial perfusion with ice-cold PBS and 4% PFA. Brains were collected, then dehydrated in sucrose and embedded and flash-frozen in optimal cutting temperature compound (Fisher Healthcare, SGN4585), or submerged in 70% HistoPrep ethanol (Fisher Scientific, HC1000) and paraffin embedded. Cryo-sectioned tissues were used for day 4 immunohistochemistry, and paraffin-sectioned tissues were used for endpoint immunohistochemistry and haematoxylin-and-eosin staining. Haematoxylin-and-eosin images were acquired using the Nikon Eclipse E1000 microscope. Fluorescence images were acquired using a spinning disk confocal microscope (Quorum) with 10×/0.4 NA, 40×/1.3 NA or 63×/1.4 NA objective and Volocity (Quorum, version 6.3.1). Quantification was performed using Volocity (Quorum, version 6.3.1) and ImageJ (version 1.54d). Tumour solidity was measured by calculating the ratio of the tumour area (marked by STEM121) to the area of the tumour convex hull. Circularity was calculated using the caveolin-1 signal.

Spinal cord dissection and optical clearing

For spinal cord dissection, mice were euthanized by intracardial perfusion with ice-cold PBS and 4% PFA. For the orthotopic xenograft experiments, mice were euthanized at humane endpoint. For the PIEZO2 knockdown intracisternal xenografts, time-matched samples were collected at the following time points: ONS76, 27 days; DAOY, 39 days; D425, 14 days. For the BAY-876 treatment experiment, time-matched samples were collected at the following time points: ONS76, 8 days; DAOY, 10 days. Dissected spinal cords were cleared by CUBIC passive immersion as previously described[45,137]. In brief, spinal cords were fixed

overnight in 4% PFA and washed 4 times over 24 h in PBS. They were then cut transversely in half, immersed in ScaleCUBIC-1 and incubated at 37 °C with gentle shaking (80 rpm). After 3 days, ScaleCUBIC-1 was replaced. After a further 3 days, cleared spinal cords were washed 4 times over 24 h in PBST and were refractive index-matched in 85% glycerol. Cleared spinal cords were stored and imaged in 85% glycerol. Imaging was performed on the Leica SP8 laser scanning confocal microscope using the 5×/0.15 NA objective and LAS X software (Leica, version 1.4.4) (orthotopic xenograft experiments) or the Zeiss Z1 light sheet microscope using the 5×/0.16 NA aqueous objective and Zen Lightsheet 2014 software (Zeiss) (intracisternal xenograft experiments). Images were acquired simultaneously using the 488 nm laser to detect ZsGreen-expressing tumour cells and 561 nm laser to detect autofluorescence. Quantification and 3D reconstruction were performed using Imaris (Oxford Instruments, version 10.1.1). A surface was created using the autofluorescence signal, which was used to mask the ZsGreen signal to obtain specific metastatic tumour signal. A surface was then created around this signal to obtain volume of metastatic tumours. 3D reconstructions were created using the surfaces of the autofluorescence signal and masked ZsGreen signal. Histograms and nonlinear regressions were generated in Prism (GraphPad, version 10.0.3).

Zebrafish xenografts

Animals were raised in accordance with the Canadian Council on Animal Care (CCAC) guidelines, and all experiments were approved under an Animal Use Protocol established with the Animal Care Committee at the Hospital for Sick Children Research Institute (AUP #1000065704). The fish used for xenograft were from a genetic in-cross of ccdc151(ts272) strain heterozygous adult zebrafish. The controls were *ccdc151* heterozygous and wild-type animals, and *ccdc151* were their homozygous siblings. Forty-eight hours post fertilization, embryos were injected with 100 ONS76 cells in 2 nl of PBS into the hindbrain using a Pneumatic PicoPump (World Precision Instruments) with a glass filament needle—1.0 OD/0.75 ID (World Precision Instruments, #TW100F-4). Five days after tumour implantation, xenografted zebrafish were fixed in 4% PFA, and depigmented and optically cleared using DEEP-Clear[138]. In brief, fixed zebrafish were treated with acetone at −20 °C overnight, washed with PBS and depigmented using 3% H_2O_2 prepared in 0.8% KOH at room temperature for 20 min. The fish were then washed with PBST, incubated in DEEP-Clear Solution-1.1 for 2.5 h at 37 °C and blocked with 10% NGS in PBST for 1 h at room temperature. They were then immunostained for 5 days with mouse anti-human nuclear antigen antibody (1:250; Thermo Fisher Scientific #MSM3-99-P0) and 5 days with Alexa Fluor 488 donkey anti-mouse IgG (1:250; Jackson Immunoresearch #715-545-151) in PBST with 5% NGS at 4 °C. The stained fish were incubated in DEEP-Clear Solution 2 until clear and then imaged using the Zeiss Z1 light sheet microscope with the 5×/0.16 NA aqueous objective and Zen Lightsheet 2014 software (Zeiss). Cleared fish were mounted in 2% agarose and imaging medium was 85% glycerol. Images were acquired simultaneously using the 488 nm laser to detect human nuclear antigen-stained tumour cells and 561 nm laser to detect autofluorescence. Quantification was performed using Imaris (Oxford Instruments, version 10.1.1) using the surface function.

Bioinformatic analysis

MB transcriptomic data and patient clinical information. Gene expression data (Affymetrix microarrays), tumour subtype information and metastatic status for 763 primary MB tumours of the SSH, WNT, Group 3 and Group 4 subtypes were downloaded from the GEO (GSE85217)[73].

Mechanosensitive ion channel gene expression in non-metastatic and metastatic MB. Mechanosensitive ion channel gene expression in the MB cohort from Cavalli et al.[73] was compared between primary tumours without metastasis and tumours with reported metastasis. For each MB subtype, samples were classified into two groups based on the reported patient metastasis. Differential expression between these two tumour types was calculated using Mann–Whitney *U*-tests.

Analysis of *PIEZO1* and *PIEZO2* expression in human SHH MB and normal cerebellum tissue. Processed transcriptomic data were downloaded from the GEO repository (accession number GSE124814)[75]. A total of 23 datasets were integrated and normalized using standard protocols. To assess the expression levels of *PIEZO1* and *PIEZO2*, samples from patients classified into the SHH subgroup and normal cerebellum tissue controls were analysed. Statistical significance was determined via the Wilcoxon signed-rank test, with *P* values adjusted for multiple comparisons using the Bonferroni correction method.

Analysis of public scRNA-seq data. scRNA-seq expression data and metadata of human MB were retrieved from the GEO with accession number GSE119926, raw count of each cell was preprocessed with Seurat (v5.1.0)[139], and the low-quality cell with nFeature_RNA <2,500 and single cells from patient-derived xenografts were removed from subsequent analysis. NormalizeData was used to normalize expression data; the first 11 PCs were used in the functions FindNeighbors and RunUMAP. *PIEZO2*$^+$ cells were defined as those in which at least one raw expression count of the *PIEZO2* gene was detected, while *PIEZO2*$^-$ cells were characterized by the absence of detectable *PIEZO2* expression.

Magnetic resonance imaging of patients with MB. The magnetic resonance imaging procedures of patients with MB were approved by the Xiangya Hospital Ethics Committee (#202404080). For CSF flow and pressure simulation, contrast-enhanced T1-weighted MRIs of 10 patients diagnosed with MB were collected from Xiangya Hospital spanning the period between 2014 and 2023. The boundaries of the 4th ventricle and the margins of MB tumours on these scans were defined and labelled by a neurosurgeon and a radiologist. For spinal metastasis quantification, MRIs for 88 patients diagnosed with MB were collected from Xiangya Hospital spanning the period between 2016 and 2023. The presence of metastasis was determined based on postoperative spinal cord MRI and follow-up data, while preoperative head MRI was used to assess the degree of compression. All evaluations were performed by a radiologist in conjunction with two neurosurgeons.

Finite element simulation of CSF flow. A computational model was developed using COMSOL Multiphysics 5.4 to simulate the CSF within a tumour-obstructed conduit[43]. The two-dimensional simulation model was built with CSF conduit geometries as previously shown[43]. A spherical blockage mimicking tumour was added to the CSF conduit at the cervicomedullary junction, taking up the conduit space from 0% to 95%. The zero-displacement boundary condition was imposed at the surface of the CSF conduit. The CSF within the conduit was assigned to be moving liquid, with a density of 1,000 kg m^{-3}, a viscosity of 0.00103 Pa s and a Poisson ratio of 0.49. The inlet was defined within the lateral ventricle, whereas the outlet was defined in the 4th ventricle. The mass flow inlet boundary condition with bulk production of 500 ml per day (that is, 6.25×10^{-6} kg s^{-1}) was used to mimic patient CSF flow. The COMSOL default mesh was used. The shear stress on the CSF conduit, the pressure and the flow velocity within the conduit were recorded. The simulation project file is available at https://github.com/XianShawn/CSF-Simulation.

Statistics and reproducibility. The statistical test used and the number of biologically independent replicates are indicated in the accompanying figure legends. All statistical tests were performed using Prism (GraphPad, version 10.0.3). No statistical method was used to predetermine sample size. However, sample sizes are consistent with those reported in previous publications[124,140]. No data were excluded from the analyses. For animal experiments, mice with the same gender

and age were divided randomly into experimental groups. Blinding was applied for imaging of cleared spinal cords and quantification of glucose uptake, cell clustering and cell–cell junctional intensity. Where blinding was not applied, quantification was performed using software calculated automatic thresholds and standardized regions of interest across experimental groups.

Reporting summary

Further information on research design is available in the Nature Portfolio Reporting Summary linked to this article.

Data availability

The main data supporting the results in this study and source data are available within the paper and its Supplementary Information. The CSF flow simulation project file is available at https://github.com/XianShawn/CSF-Simulation. Gene expression data (Affymetrix microarrays), tumour subtype information and metastatic status for 763 primary medulloblastoma tumours of the SSH, WNT, Group 3 and Group 4 subtypes were downloaded from the Gene Expression Omnibus (GEO; GSE85217)[73]. Gene expression data for *PIEZO1* and *PIEZO2* expression analysis in SHH MB and normal cerebellum were downloaded from GEO (GSE124814). scRNA-seq expression data and metadata of human MB were retrieved from GEO (GSE119926). RNA-seq data of static and FSS-treated MB cells were deposited to GEO (GSE288458)[135]. RNA-seq reads were aligned to GRCh38. Source data are provided with this paper.

References

1. Lambert, A. W., Pattabiraman, D. R. & Weinberg, R. A. Emerging biological principles of metastasis. *Cell* **168**, 670–691 (2017).
2. Northcott, J. M., Dean, I. S., Mouw, J. K. & Weaver, V. M. Feeling stress: the mechanics of cancer progression and aggression. *Front. Cell Dev. Biol.* **6**, 17 (2018).
3. Momin, A. et al. Channeling force in the brain: mechanosensitive ion channels choreograph mechanics and malignancies. *Trends Pharmacol. Sci.* **42**, 367–384 (2021).
4. Broders-Bondon, F., Nguyen Ho-Bouldoires, T. H., Fernandez-Sanchez, M.-E. & Farge, E. Mechanotransduction in tumor progression: the dark side of the force. *J. Cell Biol.* **217**, 1571–1587 (2018).
5. Padera, T. P. et al. Cancer cells compress intratumour vessels. *Nature* **427**, 695 (2004).
6. Paszek, M. J. et al. Tensional homeostasis and the malignant phenotype. *Cancer Cell* **8**, 241–254 (2005).
7. Levental, K. R. et al. Matrix crosslinking forces tumor progression by enhancing integrin signaling. *Cell* **139**, 891–906 (2009).
8. Krndija, D. et al. Substrate stiffness and the receptor-type tyrosine-protein phosphatase alpha regulate spreading of colon cancer cells through cytoskeletal contractility. *Oncogene* **29**, 2724–2738 (2010).
9. Samuel, M. S. et al. Actomyosin-mediated cellular tension drives increased tissue stiffness and β-catenin activation to induce epidermal hyperplasia and tumor growth. *Cancer Cell* **19**, 776–791 (2011).
10. Chauhan, V. P. et al. Angiotensin inhibition enhances drug delivery and potentiates chemotherapy by decompressing tumour blood vessels. *Nat. Commun.* **4**, 2516 (2013).
11. Calvo, F. et al. Mechanotransduction and YAP-dependent matrix remodelling is required for the generation and maintenance of cancer-associated fibroblasts. *Nat. Cell Biol.* **15**, 637–646 (2013).
12. Galie, P. A. et al. Fluid shear stress threshold regulates angiogenic sprouting. *Proc. Natl Acad. Sci. USA* **111**, 7968–7973 (2014).
13. Fernández-Sánchez, M. E. et al. Mechanical induction of the tumorigenic β-catenin pathway by tumour growth pressure. *Nature* **523**, 92–95 (2015).
14. Miroshnikova, Y. A. et al. Tissue mechanics promote IDH1-dependent HIF1α–tenascin C feedback to regulate glioblastoma aggression. *Nat. Cell Biol.* **18**, 1336–1345 (2016).
15. Bordeleau, F. et al. Matrix stiffening promotes a tumor vasculature phenotype. *Proc. Natl Acad. Sci. USA* **114**, 492–497 (2017).
16. Chen, X. et al. A feedforward mechanism mediated by mechanosensitive ion channel PIEZO1 and tissue mechanics promotes glioma aggression. *Neuron* **100**, 799–815.e7 (2018).
17. Barnes, J. M. et al. A tension-mediated glycocalyx–integrin feedback loop promotes mesenchymal-like glioblastoma. *Nat. Cell Biol.* **20**, 1203–1214 (2018).
18. Pankova, D. et al. RASSF1A controls tissue stiffness and cancer stem-like cells in lung adenocarcinoma. *EMBO J.* **38**, e100532 (2019).
19. Lee, J. Y. et al. YAP-independent mechanotransduction drives breast cancer progression. *Nat. Commun.* **10**, 1848 (2019).
20. Chen, X. et al. Mechanosensitive brain tumor cells construct blood-tumor barrier to mask chemosensitivity. *Neuron* **111**, 30–48. e14 (2023).
21. Northey, J. J. et al. Mechanosensitive hormone signaling promotes mammary progenitor expansion and breast cancer risk. *Cell Stem Cell* **31**, 106–126.e13 (2024).
22. Wirtz, D., Konstantopoulos, K. & Searson, P. C. The physics of cancer: the role of physical interactions and mechanical forces in metastasis. *Nat. Rev. Cancer* **11**, 512–522 (2011).
23. Follain, G. et al. Fluids and their mechanics in tumour transit: shaping metastasis. *Nat. Rev. Cancer* **20**, 107–124 (2020).
24. Wei, S. C. et al. Matrix stiffness drives epithelial–mesenchymal transition and tumour metastasis through a TWIST1–G3BP2 mechanotransduction pathway. *Nat. Cell Biol.* **17**, 678–688 (2015).
25. Fattet, L. et al. Matrix rigidity controls epithelial-mesenchymal plasticity and tumor metastasis via a mechanoresponsive EPHA2/LYN complex. *Dev. Cell* **54**, 302–316.e7 (2020).
26. Fanfone, D. et al. Confined migration promotes cancer metastasis through resistance to anoikis and increased invasiveness. *eLife* **11**, e73150 (2022).
27. Follain, G. et al. Hemodynamic forces tune the arrest, adhesion, and extravasation of circulating tumor cells. *Dev. Cell* **45**, 33–52. e12 (2018).
28. Hovestadt, V. et al. Medulloblastomics revisited: biological and clinical insights from thousands of patients. *Nat. Rev. Cancer* **20**, 42–56 (2020).
29. Ostrom, Q. T. et al. CBTRUS Statistical Report: primary brain and other central nervous system tumors diagnosed in the United States in 2010–2014. *Neuro Oncol.* **19**, v1–v88 (2017).
30. Ramaswamy, V. et al. Recurrence patterns across medulloblastoma subgroups: an integrated clinical and molecular analysis. *Lancet Oncol.* **14**, 1200–1207 (2013).
31. Fults, D. W., Taylor, M. D. & Garzia, L. Leptomeningeal dissemination: a sinister pattern of medulloblastoma growth. *J. Neurosurg. Pediatr.* **23**, 613–621 (2019).
32. Cocito, C. et al. Leptomeningeal dissemination in pediatric brain tumors. *Neoplasia* **39**, 100898 (2023).
33. Garzia, L. et al. A hematogenous route for medulloblastoma leptomeningeal metastases. *Cell* **173**, 1549 (2018).
34. Wu, X. et al. Clonal selection drives genetic divergence of metastatic medulloblastoma. *Nature* **482**, 529–533 (2012).
35. Morrissy, A. S. et al. Divergent clonal selection dominates medulloblastoma at recurrence. *Nature* **529**, 351–357 (2016).
36. Martirosian, V. et al. Medulloblastoma uses GABA transaminase to survive in the cerebrospinal fluid microenvironment and promote leptomeningeal dissemination. *Cell Rep.* **35**, 109302 (2021).
37. Kahn, S. A. et al. Notch1 regulates the initiation of metastasis and self-renewal of Group 3 medulloblastoma. *Nat. Commun.* **9**, 4121 (2018).

38. Kelley, D. H. & Thomas, J. H. Cerebrospinal fluid flow. *Annu. Rev. Fluid Mech.* **55**, 237–264 (2023).
39. Yamada, S. et al. Quantification of oscillatory shear stress from reciprocating CSF motion on 4D flow imaging. *Am. J. Neuroradiol.* **42**, 479–486 (2021).
40. Jiang, T. et al. Impact of tumor location and fourth ventricle infiltration in medulloblastoma. *Acta Neurochir.* **158**, 1187–1195 (2016).
41. Meyers, S. P., Kemp, S. S. & Tarr, R. W. MR imaging features of medulloblastomas. *Am. J. Roentgenol.* **158**, 859–865 (1992).
42. Lee, M., Wisoff, J. H., Abbott, R., Freed, D. & Epstein, F. J. Management of hydrocephalus in children with medulloblastoma: prognostic factors for shunting. *Pediatr. Neurosurg.* **20**, 240–247 (1994).
43. Ul Haq, U. et al. Computational modeling and simulation of stenosis of the cerebral aqueduct due to brain tumor. *Eng. Appl. Comput. Fluid Mech.* **16**, 1018–1030 (2022).
44. Vandenbulcke, S., De Pauw, T., Dewaele, F., Degroote, J. & Segers, P. Computational fluid dynamics model to predict the dynamical behavior of the cerebrospinal fluid through implementation of physiological boundary conditions. *Front. Bioeng. Biotechnol.* **10**, 1040517 (2022).
45. Liang, H., Schofield, E. & Paxinos, G. Imaging serotonergic fibers in the mouse spinal cord using the CLARITY/CUBIC technique. *J. Vis. Exp.* **26**, 53673 (2016).
46. Yan, C. et al. Visualizing engrafted human cancer and therapy responses in immunodeficient zebrafish. *Cell* **177**, 1903–1914.e14 (2019).
47. van Bree, N. et al. Development of an orthotopic medulloblastoma zebrafish model for rapid drug testing. *Neuro Oncol.* **27**, 779–794 (2025).
48. Hjeij, R. et al. CCDC151 mutations cause primary ciliary dyskinesia by disruption of the outer dynein arm docking complex formation. *Am. J. Hum. Genet.* **95**, 257–274 (2014).
49. Jerber, J. et al. The coiled-coil domain containing protein CCDC151 is required for the function of IFT-dependent motile cilia in animals. *Hum. Mol. Genet.* **23**, 563–577 (2014).
50. Grimes, D. T. et al. Zebrafish models of idiopathic scoliosis link cerebrospinal fluid flow defects to spine curvature. *Science* **352**, 1341–1344 (2016).
51. Christ, K. V., Williamson, K. B., Masters, K. S. & Turner, K. T. Measurement of single-cell adhesion strength using a microfluidic assay. *Biomed. Microdevices* **12**, 443–455 (2010).
52. Lu, H. et al. Microfluidic shear devices for quantitative analysis of cell adhesion. *Anal. Chem.* **76**, 5257–5264 (2004).
53. Kane, M. A. et al. Adhesion strength of tumor cells predicts metastatic disease in vivo. *Cell Rep.* **44**, 115359 (2025).
54. Fuhrmann, A., Banisadr, A., Beri, P., Tlsty, T. D. & Engler, A. J. Metastatic state of cancer cells may be indicated by adhesion strength. *Biophys. J.* **112**, 736–745 (2017).
55. King, M. R. *Principles of Cellular Engineering: Understanding the Biomolecular Interface* (Elsevier Academic Press, 2006).
56. Borsig, L. Selectins in cancer immunity. *Glycobiology* **28**, 648–655 (2018).
57. Läubli, H. & Borsig, L. Selectins promote tumor metastasis. *Semin. Cancer Biol.* **20**, 169–177 (2010).
58. Katayama, Y., Hidalgo, A., Chang, J., Peired, A. & Frenette, P. S. CD44 is a physiological E-selectin ligand on neutrophils. *J. Exp. Med.* **201**, 1183–1189 (2005).
59. Dimitroff, C. J., Lee, J. Y., Rafii, S., Fuhlbrigge, R. C. & Sackstein, R. CD44 is a major E-selectin ligand on human hematopoietic progenitor cells. *J. Cell Biol.* **153**, 1277–1286 (2001).
60. Pandya, P., Orgaz, J. L. & Sanz-Moreno, V. Modes of invasion during tumour dissemination. *Mol. Oncol.* **11**, 5–27 (2017).
61. Murrell, M., Oakes, P. W., Lenz, M. & Gardel, M. L. Forcing cells into shape: the mechanics of actomyosin contractility. *Nat. Rev. Mol. Cell Biol.* **16**, 486–498 (2015).
62. Spector, R., Robert Snodgrass, S. & Johanson, C. E. A balanced view of the cerebrospinal fluid composition and functions: focus on adult humans. *Exp. Neurol.* **273**, 57–68 (2015).
63. Roche, S., Gabelle, A. & Lehmann, S. Clinical proteomics of the cerebrospinal fluid: towards the discovery of new biomarkers. *Proteomics Clin. Appl.* **2**, 428–436 (2008).
64. Leen, W. G., Willemsen, M. A., Wevers, R. A. & Verbeek, M. M. Cerebrospinal fluid glucose and lactate: age-specific reference values and implications for clinical practice. *PLoS ONE* **7**, e42745 (2012).
65. Salvi, A. M., Bays, J. L., Mackin, S. R., Mege, R.-M. & DeMali, K. A. Ankyrin G organizes membrane components to promote coupling of cell mechanics and glucose uptake. *Nat. Cell Biol.* **23**, 457–466 (2021).
66. Abramczyk, H. & Imiela, A. The biochemical, nanomechanical and chemometric signatures of brain cancer. *Spectrochim. Acta A* **188**, 8–19 (2018).
67. Kornberg, L., Earp, H. S., Parsons, J. T., Schaller, M. & Juliano, R. L. Cell adhesion or integrin clustering increases phosphorylation of a focal adhesion-associated tyrosine kinase. *J. Biol. Chem.* **267**, 23439–23442 (1992).
68. Hanks, S. K., Calalb, M. B., Harper, M. C. & Patel, S. K. Focal adhesion protein-tyrosine kinase phosphorylated in response to cell attachment to fibronectin. *Proc. Natl Acad. Sci. USA* **89**, 8487–8491 (1992).
69. Laklai, H. et al. Genotype tunes pancreatic ductal adenocarcinoma tissue tension to induce matricellular fibrosis and tumor progression. *Nat. Med.* **22**, 497–505 (2016).
70. Long, K., Moss, L., Laursen, L., Boulter, L. & Ffrench-Constant, C. Integrin signalling regulates the expansion of neuroepithelial progenitors and neurogenesis via Wnt7a and Decorin. *Nat. Commun.* **7**, 10354 (2016).
71. Calderwood, S. K., Khaleque, M. A., Sawyer, D. B. & Ciocca, D. R. Heat shock proteins in cancer: chaperones of tumorigenesis. *Trends Biochem. Sci.* **31**, 164–172 (2006).
72. Zeng, Q. et al. Synaptic proximity enables NMDAR signalling to promote brain metastasis. *Nature* **573**, 526–531 (2019).
73. Cavalli, F. M. G. et al. Intertumoral heterogeneity within medulloblastoma subgroups. *Cancer Cell* **31**, 737–754.e6 (2017).
74. Szczot, M., Nickolls, A. R., Lam, R. M. & Chesler, A. T. The form and function of PIEZO2. *Annu. Rev. Biochem.* **90**, 507–534 (2021).
75. Weishaupt, H. et al. Batch-normalization of cerebellar and medulloblastoma gene expression datasets utilizing empirically defined negative control genes. *Bioinformatics* **35**, 3357–3364 (2019).
76. Hovestadt, V. et al. Resolving medulloblastoma cellular architecture by single-cell genomics. *Nature* **572**, 74–79 (2019).
77. Pardo-Pastor, C. et al. Piezo2 channel regulates RhoA and actin cytoskeleton to promote cell mechanobiological responses. *Proc. Natl Acad. Sci. USA* **115**, 1925–1930 (2018).
78. Choi, S. A. et al. In vivo bioluminescence imaging for leptomeningeal dissemination of medulloblastoma in mouse models. *BMC Cancer* **16**, 723 (2016).
79. Surcel, A. & Robinson, D. N. Meddling with myosin's mechanobiology in cancer. *Proc. Natl Acad. Sci. USA* **116**, 15322–15323 (2019).
80. Siebeneicher, H. et al. Identification and optimization of the first highly selective GLUT1 inhibitor BAY-876. *ChemMedChem* **11**, 2261–2271 (2016).
81. Ranade, S. S. et al. Piezo1, a mechanically activated ion channel, is required for vascular development in mice. *Proc. Natl Acad. Sci. USA* https://doi.org/10.1073/pnas.1409233111 (2014).

82. Li, J. et al. Piezo1 integration of vascular architecture with physiological force. *Nature* **515**, 279–282 (2014).
83. Wang, S. et al. Endothelial cation channel PIEZO1 controls blood pressure by mediating flow-induced ATP release. *J. Clin. Invest.* **126**, 4527–4536 (2016).
84. Choi, D. et al. Piezo1-regulated mechanotransduction controls flow-activated lymphatic expansion. *Circ. Res.* **131**, e2–e21 (2022).
85. Carrisoza-Gaytan, R. et al. PIEZO1 is a distal nephron mechanosensor and is required for flow-induced K^+ secretion. *J. Clin. Invest.* **134**, e174806 (2024).
86. Ranade, S. S. et al. Piezo2 is the major transducer of mechanical forces for touch sensation in mice. *Nature* **516**, 121–125 (2014).
87. Murthy, S. E. et al. The mechanosensitive ion channel Piezo2 mediates sensitivity to mechanical pain in mice. *Sci. Transl. Med.* **10**, eaat9897 (2018).
88. Woo, S. H. et al. Piezo2 is the principal mechanotransduction channel for proprioception. *Nat. Neurosci.* **18**, 1756–1762 (2015).
89. Tian, S. et al. Loss of lung microvascular endothelial Piezo2 expression impairs NO synthesis, induces EndMT, and is associated with pulmonary hypertension. *Am. J. Physiol. Circ. Physiol.* **323**, H958–H974 (2022).
90. Nonomura, K. et al. Piezo2 senses airway stretch and mediates lung inflation-induced apnoea. *Nature* **541**, 176–181 (2017).
91. Marshall, K. L. et al. PIEZO2 in sensory neurons and urothelial cells coordinates urination. *Nature* **588**, 290–295 (2020).
92. Linninger, A. A. et al. A mathematical model of blood, cerebrospinal fluid and brain dynamics. *J. Math. Biol.* **59**, 729–759 (2009).
93. Linninger, A. A. et al. Cerebrospinal fluid flow in the normal and hydrocephalic human brain. *IEEE Trans. Biomed. Eng.* **54**, 291–302 (2007).
94. Sweetman, B. & Linninger, A. A. Cerebrospinal fluid flow dynamics in the central nervous system. *Ann. Biomed. Eng.* **39**, 484–496 (2011).
95. Pahlavian, S. H., Loth, F., Luciano, M., Oshinski, J. & Martin, B. A. Neural tissue motion impacts cerebrospinal fluid dynamics at the cervical medullary junction: a patient-specific moving-boundary computational model. *Ann. Biomed. Eng.* **43**, 2911–2923 (2015).
96. Siyahhan, B. et al. Flow induced by ependymal cilia dominates near-wall cerebrospinal fluid dynamics in the lateral ventricles. *J. R. Soc. Interface* **11**, 8–10 (2014).
97. Bothwell, S. W., Janigro, D. & Patabendige, A. Cerebrospinal fluid dynamics and intracranial pressure elevation in neurological diseases. *Fluids Barriers CNS* **16**, 1–18 (2019).
98. Thomas, J. H. Fluid dynamics of cerebrospinal fluid flow in perivascular spaces. *J. R. Soc. Interface* **16**, 20190572 (2019).
99. Balasundaram, H., Sathyamoorthi, S., Fernandez-Gamiz, U., Noeiaghdam, S. & Santra, S. S. Hydrocephalic cerebrospinal fluid flowing rotationally with pulsatile boundaries: a mathematical simulation of the thermodynamical approach. *Theor. Appl. Mech. Lett.* **13**, 100418 (2023).
100. Lehner, K. R., Jiang, K., Rincon-Torroella, J., Perera, R. & Bettegowda, C. Cerebrospinal fluid biomarkers in pediatric brain tumors: a systematic review. *Neoplasia* **35**, 100852 (2023).
101. Hollister, J. C. P. et al. Shear thinning behavior of cerebrospinal fluid with elevated protein or cellular concentration. *Front. Phys.* **11**, 1308136 (2023).
102. King, M. R. in *Heat Transfer and Fluid Flow in Minichannels and Microchannels* (eds Kandlikar, S. G. et al.) 409–442 (Elsevier Science Ltd., 2006).
103. Ma, S. et al. Excessive mechanotransduction in sensory neurons causes joint contractures. *Science* **379**, 201–206 (2023).
104. Vander Heiden, M. G., Cantley, L. C. & Thompson, C. B. Understanding the Warburg effect: the metabolic requirements of cell proliferation. *Science* **324**, 1029–1033 (2009).
105. Temre, M. K., Kumar, A. & Singh, S. M. An appraisal of the current status of inhibition of glucose transporters as an emerging antineoplastic approach: promising potential of new pan-GLUT inhibitors. *Front. Pharmacol.* **13**, 1035510 (2022).
106. Peng, W. et al. Glucose transporter 3 in neuronal glucose metabolism: health and diseases. *Metabolism* **123**, 154869 (2021).
107. Liu, Y. et al. A small-molecule inhibitor of glucose transporter 1 downregulates glycolysis, induces cell-cycle arrest, and inhibits cancer cell growth in vitro and in vivo. *Mol. Cancer Ther.* **11**, 1672–1682 (2012).
108. Chan, D. A. et al. Targeting GLUT1 and the Warburg effect in renal cell carcinoma by chemical synthetic lethality. *Sci. Transl. Med.* **3**, 94ra70 (2011).
109. Oechsle, K., Lange-Brock, V., Kruell, A., Bokemeyer, C. & de Wit, M. Prognostic factors and treatment options in patients with leptomeningeal metastases of different primary tumors: a retrospective analysis. *J. Cancer Res. Clin. Oncol.* **136**, 1729–1735 (2010).
110. Boire, A. et al. Complement component 3 adapts the cerebrospinal fluid for leptomeningeal metastasis. *Cell* **168**, 1101–1113.e13 (2017).
111. Chi, Y. et al. Cancer cells deploy lipocalin-2 to collect limiting iron in leptomeningeal metastasis. *Science* **369**, 276–282 (2020).
112. Knoblauch, S. V. et al. Chemical activation and mechanical sensitization of Piezo1 enhance TRAIL-mediated apoptosis in glioblastoma cells. *ACS Omega* **8**, 16975–16986 (2023).
113. Hope, J. M., Lopez-Cavestany, M., Wang, W., Reinhart-King, C. A. & King, M. R. Activation of Piezo1 sensitizes cells to TRAIL-mediated apoptosis through mitochondrial outer membrane permeability. *Cell Death Dis.* **10**, 837 (2019).
114. Cao, T. M. & King, M. R. Supercharged eGFP-TRAIL decorated NETs to ensnare and kill disseminated tumor cells. *Cell. Mol. Bioeng.* **13**, 359–367 (2020).
115. Zhang, Z. & King, M. R. Tuning of TRAIL clustering on the surface of nanoscale liposomes by phase separation. *Nanoscale Adv.* **6**, 402–405 (2024).
116. Lopez-Cavestany, M., Wright, O. A., Cassidy, A. M., Carter, A. T. & King, M. R. Dual affinity nanoparticles for the transport of therapeutics from carrier cells to target cells under physiological flow conditions. *ACS Omega* **8**, 42748–42761 (2023).
117. Ortiz-Otero, N., Marshall, J. R., Lash, B. W. & King, M. R. Platelet mediated TRAIL delivery for efficiently targeting circulating tumor cells. *Nanoscale Adv.* **2**, 3942–3953 (2020).
118. Greenlee, J. D., Zhang, Z., Subramanian, T., Liu, K. & King, M. R. TRAIL-conjugated liposomes that bind natural killer cells to induce colorectal cancer cell apoptosis. *J. Biomed. Mater. Res. A* **112**, 110–120 (2024).
119. Jyotsana, N., Zhang, Z., Himmel, L. E., Yu, F. & King, M. R. Minimal dosing of leukocyte targeting TRAIL decreases triple-negative breast cancer metastasis following tumor resection. *Sci. Adv.* **5**, eaaw4197 (2025).
120. Mitchell, M. J., Wayne, E., Rana, K., Schaffer, C. B. & King, M. R. TRAIL-coated leukocytes that kill cancer cells in the circulation. *Proc. Natl Acad. Sci. USA* **111**, 930–935 (2014).
121. Hendrikse, L. D. et al. Failure of human rhombic lip differentiation underlies medulloblastoma formation. *Nature* **609**, 1021–1028 (2022).
122. Vladoiu, M. C. et al. Childhood cerebellar tumours mirror conserved fetal transcriptional programs. *Nature* **572**, 67–73 (2019).
123. Smith, K. S. et al. Unified rhombic lip origins of group 3 and group 4 medulloblastoma. *Nature* **609**, 1012–1020 (2022).
124. Zou, H. et al. A neurodevelopmental epigenetic programme mediated by SMARCD3–DAB1–Reelin signalling is hijacked to promote medulloblastoma metastasis. *Nat. Cell Biol.* **25**, 493–507 (2023).

125. Lawton, A. K. et al. Cerebellar folding is initiated by mechanical constraints on a fluid-like layer without a cellular pre-pattern. *eLife* **8**, e45019 (2019).
126. Yamada, M. et al. [Establishment and biological characterization of human medulloblastoma cell lines]. *No To Shinkei* **41**, 695–702 (1989).
127. Bigner, S. H., Friedman, H. S., Vogelstein, B., Oakes, W. J. & Bigner, D. D. Amplification of the c-myc gene in human medulloblastoma cell lines and xenografts. *Cancer Res.* **50**, 2347–2350 (1990).
128. Kim, L., Toh, Y. C., Voldman, J. & Yu, H. A practical guide to microfluidic perfusion culture of adherent mammalian cells. *Lab Chip* **7**, 681–694 (2007).
129. Dong, W. et al. A designer peptide against the EAG2–Kvβ2 potassium channel targets the interaction of cancer cells and neurons to treat glioblastoma. *Nat. Cancer* **4**, 1418–1436 (2023).
130. Kim, D., Paggi, J. M., Park, C., Bennett, C. & Salzberg, S. L. Graph-based genome alignment and genotyping with HISAT2 and HISAT-genotype. *Nat. Biotechnol.* **37**, 907–915 (2019).
131. Liao, Y., Smyth, G. K. & Shi, W. The R package Rsubread is easier, faster, cheaper and better for alignment and quantification of RNA sequencing reads. *Nucleic Acids Res.* **47**, e47 (2019).
132. Love, M. I., Huber, W. & Anders, S. Moderated estimation of fold change and dispersion for RNA-seq data with DESeq2. *Genome Biol.* **15**, 550 (2014).
133. Yu, G., Wang, L.-G., Han, Y. & He, Q.-Y. clusterProfiler: an R package for comparing biological themes among gene clusters. *OMICS* **16**, 284–287 (2012).
134. Gu, Z. Complex heatmap visualization. *iMeta* **1**, e43 (2022).
135. Yang, Q., Min, H.-K., Zhao, H. & Huang, X. Fluid shear stress activates a targetable mechano-metastatic cascade to promote medulloblastoma metastasis. *NCBI GEO* https://www.ncbi.xyz/geo/query/acc.cgi?acc=GSE288458 (2025).
136. Law, V. et al. A murine Ommaya xenograft model to study direct-targeted therapy of leptomeningeal disease. *J. Vis. Exp.* https://doi.org/10.3791/62033 (2021).
137. Susaki, E. A. et al. Advanced CUBIC protocols for whole-brain and whole-body clearing and imaging. *Nat. Protoc.* **10**, 1709–1727 (2015).
138. Pende, M. et al. A versatile depigmentation, clearing, and labeling method for exploring nervous system diversity. *Sci. Adv.* **6**, eaba0365 (2025).
139. Hao, Y. et al. Dictionary learning for integrative, multimodal and scalable single-cell analysis. *Nat. Biotechnol.* **42**, 293–304 (2024).
140. Pang, R. et al. PIEZO1 mechanically regulates the antitumour cytotoxicity of T lymphocytes. *Nat. Biomed. Eng.* https://doi.org/10.1038/s41551-024-01188-5 (2024).

Acknowledgements

This work is supported by SickKids Foundation, Arthur and Sonia Labatt Brain Tumour Research Centre, Garron Family Cancer Centre, Early Researcher Award, Meagan's HUG Operating Grant (MW-2022-01) and Canadian Institute of Health Research Project Grants (506069, 406569 and 377122) to X.H. H.-K.M. and J. Chan are supported by SickKids Restracomp Scholarship and Ontario Graduate Scholarship. J.R. is supported by the New Investigator Award of the Terry Fox Research Institute (TFRI). A.B. is supported by Ontario Graduate Scholarship. X.W. is supported by Brain Tumour Foundation of Canada Dunn with Cancer Research Fellowship, SickKids Lap-Chee Tsui Fellowship and Inspiration Award from Hopper-Belmont Foundation. We thank P. Paroutis and K. Lau at SickKids Imaging Facility for help with confocal imaging and image analysis. We thank W. Wang for technical assistance. We thank Y. Shi for critical reading of the paper. Schematics were created using BioRender.com. X.H. is a catalyst scholar at The Hospital for Sick Children and Canada Research Chair in Cancer Biophysics.

Author contributions

X.H. directed the study. Experimental design, data acquisition and data analysis: H.-K.M., H.Z., J. Chan, J. Chen, E.L., S.W., L.W., X.R., H.Q., Y.S., M.N.H. and B.C. Computational analysis: A.B., X.W., S.B., R.P., Q.Y., R.D.Y.Z. and J.R. Device contributions: P.P., Y.Z. and X.L. Paper writing: H.-K.M. and X.H.

Competing interests

The authors declare no competing interests.

Additional information

Extended data is available for this paper at https://doi.org/10.1038/s41551-025-01487-5.

Supplementary information The online version contains supplementary material available at https://doi.org/10.1038/s41551-025-01487-5.

Correspondence and requests for materials should be addressed to Xi Huang.

Peer review information *Nature Biomedical Engineering* thanks Ganesh Shankar and the other, anonymous, reviewer(s) for their contribution to the peer review of this work. Peer reviewer reports are available.

Reprints and permissions information is available at www.nature.com/reprints.

Publisher's note Springer Nature remains neutral with regard to jurisdictional claims in published maps and institutional affiliations.

[1]Developmental, Stem Cell and Cancer Biology Program, The Hospital for Sick Children, Toronto, Ontario, Canada. [2]Arthur and Sonia Labatt Brain Tumour Research Centre, The Hospital for Sick Children, Toronto, Ontario, Canada. [3]Department of Molecular Genetics, University of Toronto, Toronto, Ontario, Canada. [4]Department of Neurosurgery, Xiangya Hospital, Central South University, Changsha, China. [5]Hunan International Scientific and Technological Cooperation Base of Brain Tumor Research, Xiangya Hospital, Central South University, Changsha, China. [6]Computational Biology Program, Ontario Institute for Cancer Research, Toronto, Ontario, Canada. [7]Department of Mechanical and Industrial Engineering, University of Toronto, Toronto, Ontario, Canada. [8]Institute of Robotics and Intelligent Systems, Dalian University of Technology, Dalian, China. [9]Department of Mechanical and Materials Engineering, Queen's University, Kingston, Ontario, Canada. [10]Ingenuity Labs Research Institute, Queen's University, Kingston, Ontario, Canada. [11]College of Marine Engineering, Dalian Maritime University, Dalian, China. [12]Department of Pathology, Xuanwu Hospital, Capital Medical University, Beijing, China. [13]Department of Pathology, Shengjing Hospital, China Medical University, Shenyang, China. [14]Yu-Yue Pathology Scientific Research Center and Jinfeng Laboratory, Chongqing, China. [15]Department of Medical Biophysics, University of Toronto, Toronto, Ontario, Canada. [16]Institute of Biomedical Engineering, University of Toronto, Toronto, Ontario, Canada. [17]These authors contributed equally: Hyun-Kee Min, Hongyu Zhao. ✉e-mail: xi.huang@sickkids.ca

https://doi.org/10.1038/s41551-025-01487-5

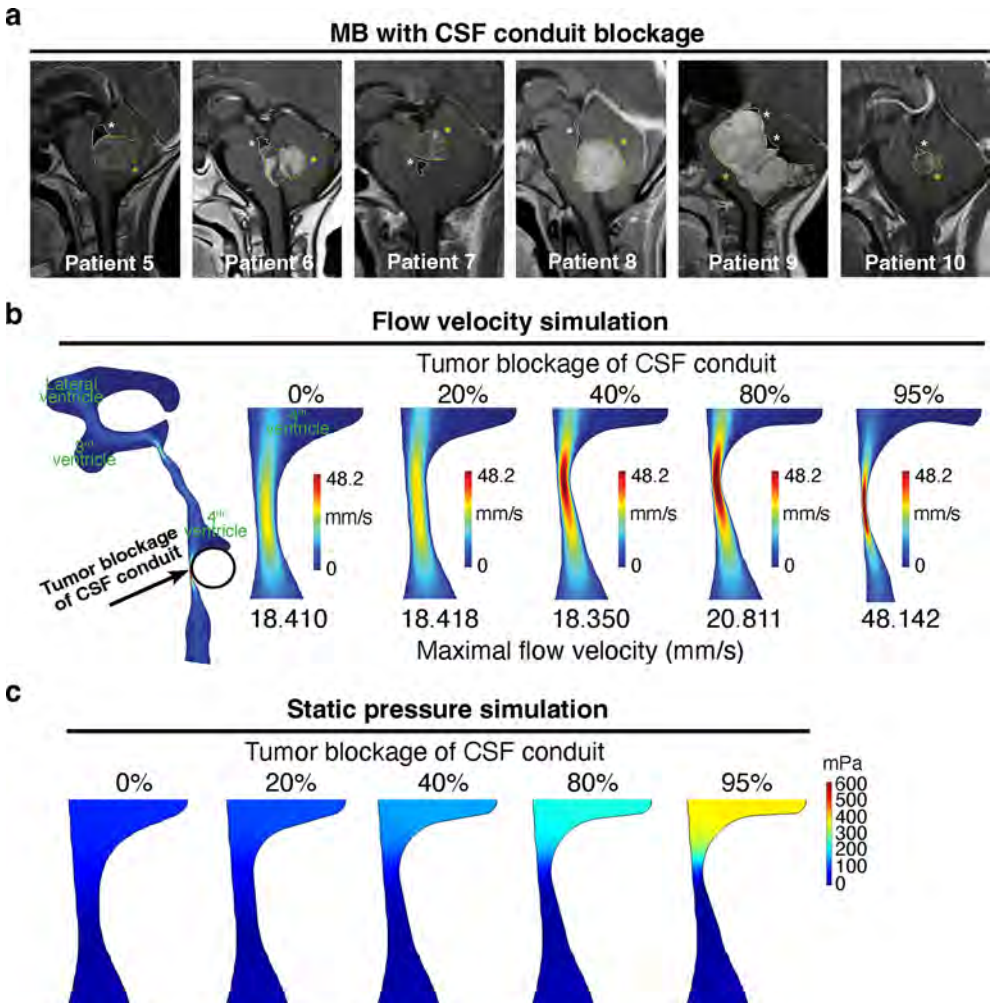

Extended Data Fig. 1 | MB magnetic resonance images and CSF flow simulation. a Magnetic resonance images of MB tumors that block CSF conduit in patients. **b** Computational simulation of CSF flow rate with various levels of MB blockage of the CSF conduit. **c** Computational simulation of pressure with various levels of MB blockage of the CSF conduit.

https://doi.org/10.1038/s41551-025-01487-5

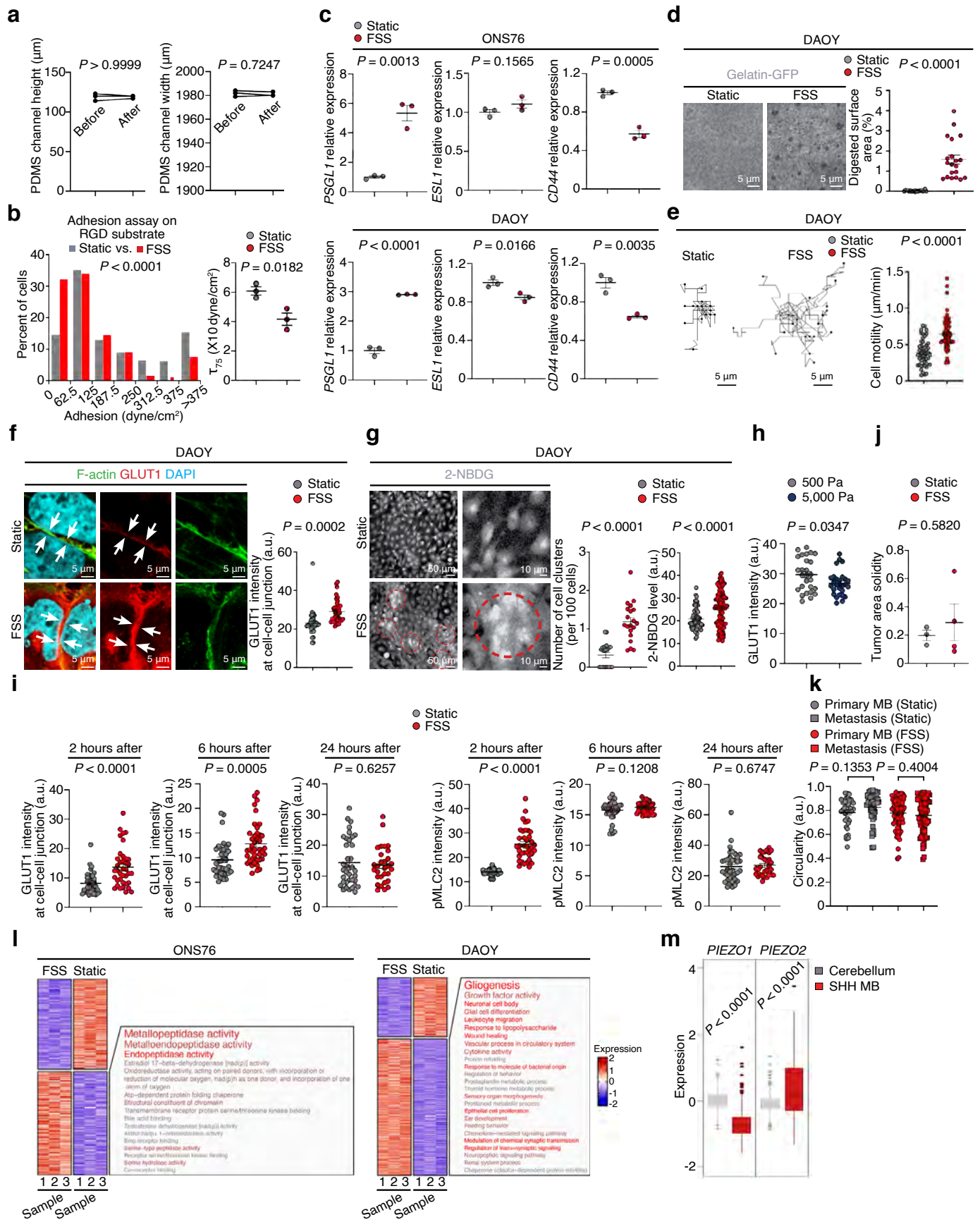

Extended Data Fig. 2 | See next page for caption.

https://doi.org/10.1038/s41551-025-01487-5

Extended Data Fig. 2 | FSS enhances ECM degradation, increases cell motility, and promotes GLUT1-mediated glucose uptake of DAOY MB cells. **a** Dimensions of three PDMS channels before and after 24 hours 70% ethanol soaking. *P* value, paired t-test. **b** Histograms of static or FSS-treated ONS76 adhesion to RGD substrate of $n = 363$ cells (Static) and $n = 330$ cells (FSS) from three independent replicates. *P* value, chi-square test. τ_{75} results of the three independent replicates are shown. *P* value, two-sided unpaired t-test. Error bars, mean ± s.e.m. **c** Expression of Selectin ligands in ONS76 and DAOY cells from three independent replicates. *P* value, two-sided unpaired t-test. Error bars, mean ± s.e.m. **d** Digested gelatin-GFP area per field-of-view of static or FSS-treated DAOY cells. $n = 20$ fields-of-view from three independent replicates. *P* value, two-sided unpaired *t*-test. Error bars, mean ± s.e.m. **e** Cell velocity of static or FSS-treated DAOY cells. $n = 50$ (static) and $n = 64$ (FSS) cells from three independent replicates. *P* value, two-sided unpaired *t*-test. Error bars, mean ± s.e.m. **f** GLUT1 intensity at cell-cell junctions of static or FSS-treated DAOY cells from $n = 34$ (static) and $n = 37$ (FSS) cell-cell junctions from three independent replicates. *P* value, two-sided unpaired *t*-test. Error bars, mean ± s.e.m. **g** Glucose uptake and cell clustering of static or FSS-treated DAOY cells. The number of cell clusters per 100 cells from $n = 20$ fields-of-view from three independent replicates (left) and 2-NBDG level in each cell from $n = 63$ (static) and $n = 103$ (FSS) cells from three independent replicates (right). *P* value, two-sided unpaired *t*-test. Error bars, mean ± s.e.m. **h** GLUT1 levels from individual ONS76 cells on stiffness substrates across $n = 27$ fields-of-view from three independent replicates. *P* value, two-sided unpaired t-test. Error bars, mean ± s.e.m. **i** FSS-induced GLUT1 cell-cell junctional enrichment and actomyosin contraction upon FSS withdrawal from $n = 39$ (2 hours after, static), $n = 38$ (2 hours after, FSS), $n = 36$ (6 hours after, static), $n = 41$ (6 hours after, FSS), $n = 37$ (24 hours after, static), and $n = 30$ (24 hours after, FSS) cells across three independent replicates. *P* value, two-sided unpaired t-test. Error bars, mean ± s.e.m. **j** Tumor cell spread of static and FSS-treated xenografts at 4 days post implantation. Results represent $n = 3$ mice (static) and $n = 4$ mice (FSS). *P* value, two-sided unpaired t-test. Error bars, mean ± s.e.m. **k** Primary and metastatic MB cell circularity from $n = 34$ cells from 3 mice (Static primary MB), $n = 44$ cells from 3 mice (Static metastasis), $n = 70$ cells from 3 mice (FSS primary MB), and $n = 75$ cells from 3 mice (FSS metastasis). *P* value, two-sided unpaired t-test. Error bars, mean ± s.e.m. **l** Differentially expressed genes and enriched pathways of MB cells. $n = 3$ biological replicates of static and FSS-treated ONS76 or DAOY cells. FSS-induced enriched pathways are labeled. **m** *PIEZO1* and *PIEZO2* expression from $n = 390$ SHH MB patient tumors and $n = 291$ normal cerebellum tissues. *P* value, two-sided Wilcoxon signed-rank test with Bonferroni correction (*PIEZO1*: $P = 8.24*10^{-79}$, *PIEZO2*: $P = 2.22*10^{-9}$). Box plots indicate interquartile range (IQR; 25th–75th percentiles) with median and 1.5x IQR whiskers.

https://doi.org/10.1038/s41551-025-01487-5

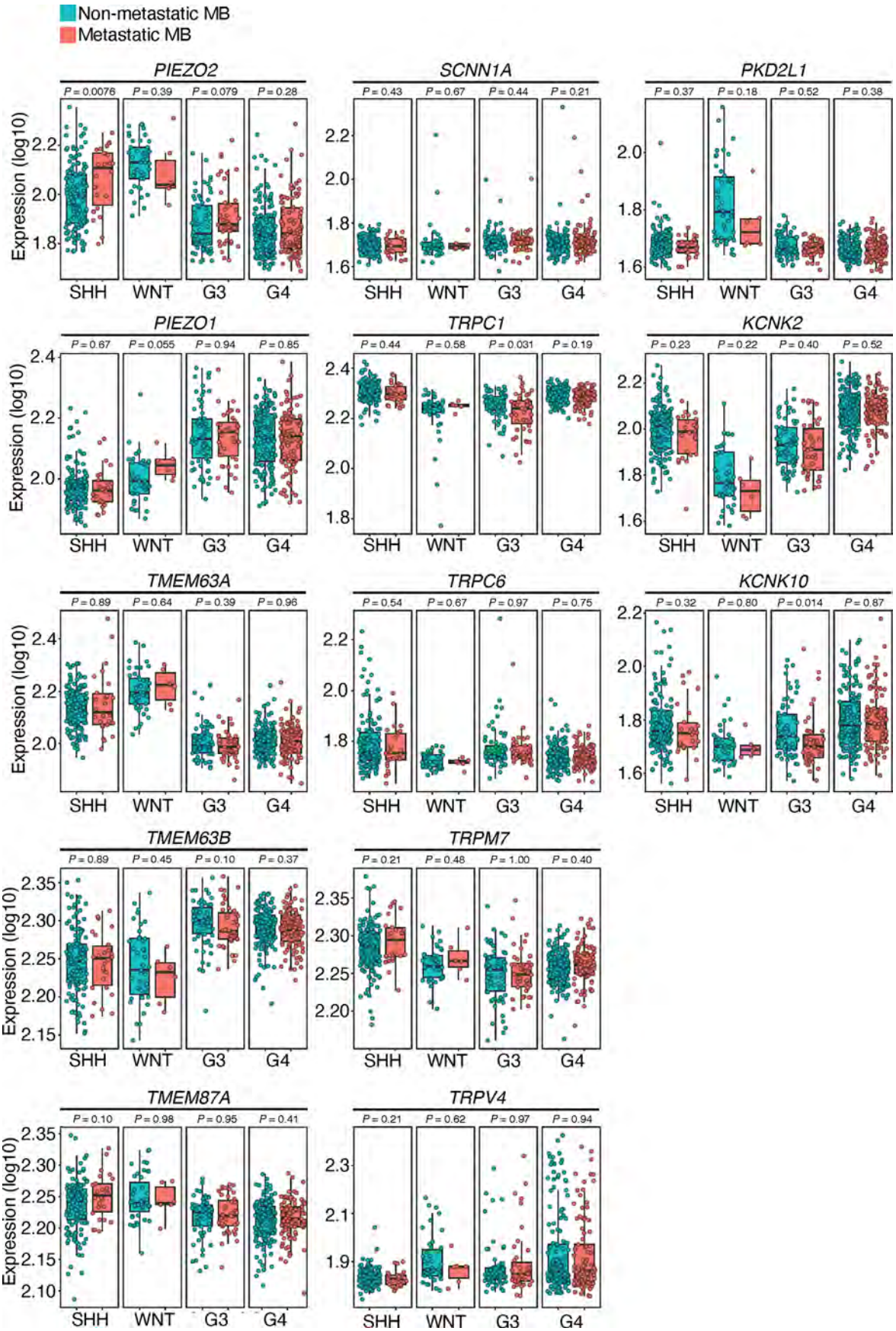

Extended Data Fig. 3 | See next page for caption.

https://doi.org/10.1038/s41551-025-01487-5

Extended Data Fig. 3 | Mechanosensitive ion channel gene expression in metastatic and non-metastatic patient MB tumors. Plots represent mechanosensitive ion channel gene expression from $n = 134$ (non-metastatic SHH MB), $n = 26$ (metastatic SHH MB), $n = 43$ (non-metastatic WNT MB), $n = 6$ (metastatic WNT MB), $n = 66$ (non-metastatic Group 3 MB), $n = 43$ (metastatic Group 3 MB), $n = 154$ (non-metastatic Group 4 MB), and $n = 101$ (metastatic Group 4 MB) patients. *P* value, two-sided Mann-Whitney U-test. Box plots indicate interquartile range (IQR; 25th–75th percentiles) with median and 1.5x IQR whiskers.

https://doi.org/10.1038/s41551-025-01487-5

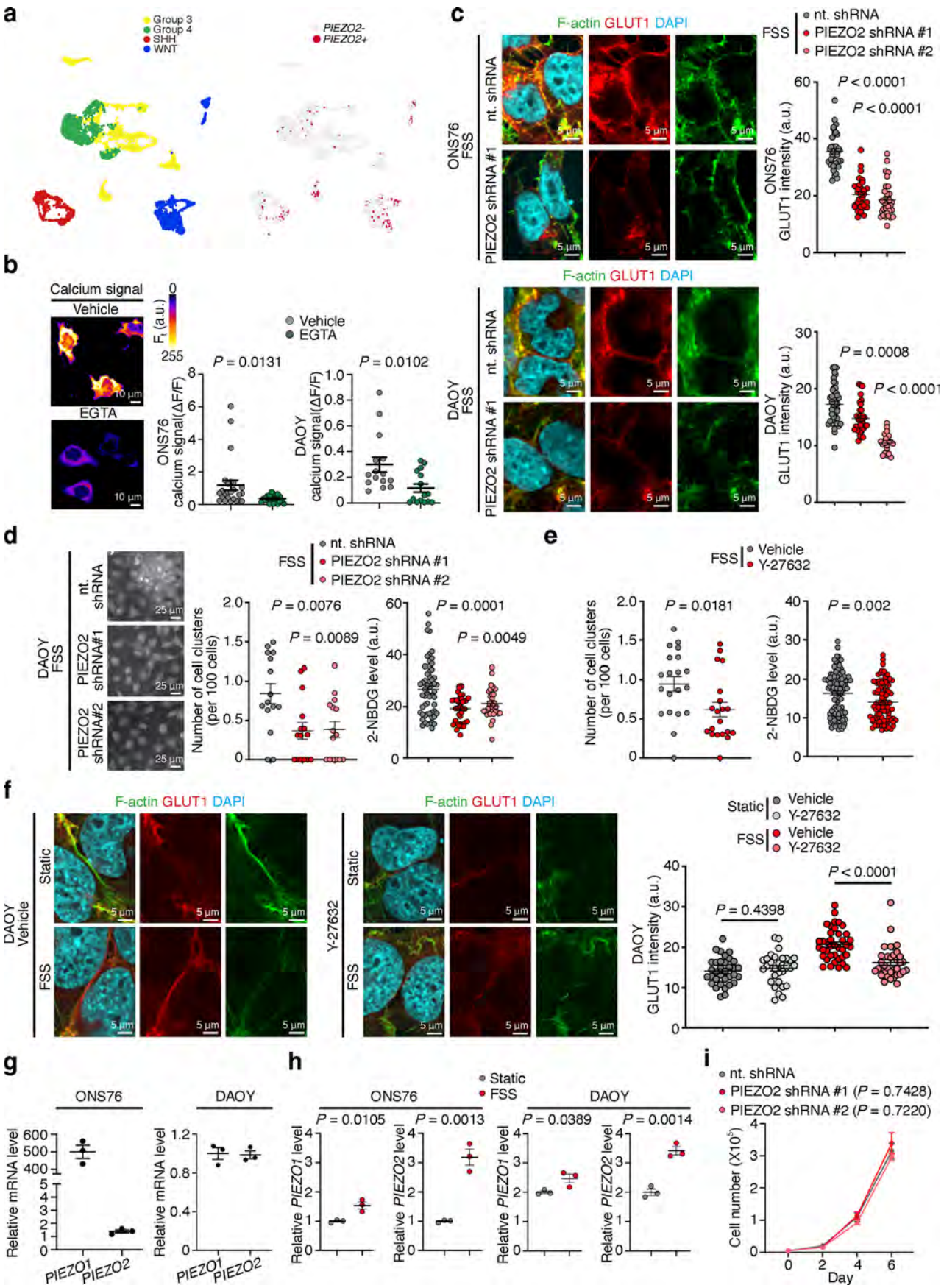

Extended Data Fig. 4 | See next page for caption.

https://doi.org/10.1038/s41551-025-01487-5

Extended Data Fig. 4 | PIEZO2 and actomyosin contractility are required for FSS-induced GLUT1 localization at cell-cell junctions and glucose uptake. **a** *PIEZO2* expression in patient MB neoplastic cells. UMAP plots of patient MB single cell RNA-sequencing data[76] shows that *PIEZO2* is expressed in the neoplastic cells of WNT, SHH, Group3, and Group 4 tumors. **b** Maximum calcium amplitudes within active compartments of FSS-treated ONS76 and DAOY cells. $n = 25$ compartments across 8 cells (ONS76 Vehicle), $n = 22$ across 9 cells (ONS76 EGTA), $n = 15$ across 9 cells (DAOY Vehicle), and $n = 15$ across 13 cells (DAOY EGTA). Results are from four independent replicates. *P* value, two-sided unpaired t-test. Error bars, mean ± s.e.m. **c** FSS-induced GLUT1 localization at the cell-cell junctions of ONS76 and DAOY cells from $n = 36$ (ONS76 nt. shRNA), $n = 30$ (ONS76 PIEZO2 shRNA #1), $n = 32$ (ONS76 PIEZO2 shRNA #2), $n = 46$ (DAOY nt. shRNA), $n = 33$ (DAOY PIEZO2 shRNA #1), and $n = 20$ (DAOY PIEZO2 shRNA #2) cell-cell junctions from three independent replicates. *P* value, two-sided unpaired *t*-test. Error bars, mean ± s.e.m. **d** The number of cell clusters per 100 cells of FSS-treated DAOY cells from $n = 15$ fields-of-view from three independent replicates (left) and 2-NBDG level in each cell from $n = 57$ (nt. shRNA), $n = 38$ (PIEZO2 shRNA #1), and $n = 37$ (PIEZO2 shRNA #2) cells from three independent replicates (right). *P* value, two-sided unpaired *t*-test. Error bars, mean ± s.e.m. **e** The number of cell clusters per 100 cells of DAOY cells treated with vehicle or Y-27632 from $n = 20$ fields-of-view from three independent replicates (left) and 2-NBDG level in each cell from $n = 118$ (Vehicle) and $n = 94$ (Y-27632) cells from three independent replicates (right). *P* value, two-sided unpaired *t*-test. Error bars, mean ± s.e.m. **f** GLUT1 intensity of DAOY cells at $n = 34$ (Static Vehicle), $n = 31$ (Static Y-27632), $n = 39$ (FSS Vehicle), and $n = 35$ (FSS Y-27632) cell-cell junctions from three independent replicates. *P* value, two-sided unpaired *t*-test. Error bars, mean ± s.e.m. **g** *PIEZO1* and *PIEZO2* expression in ONS76 and DAOY cells. Results are from three independent replicates. Error bars, mean ± s.e.m. **h** *PIEZO1* and *PIEZO2* expression was measured in static control or FSS-treated ONS76 and DAOY cells. Results are from three independent replicates. *P* value, two-sided unpaired t-test. Error bars, mean ± s.e.m. **i** PIEZO2 knockdown does not affect MB cell proliferation in the absence of FSS. ONS76 cells were cultured on 5,000 Pa stiffness gels. Results are from three independent replicates. *P* value, two-way ANOVA. Error bars, mean ± s.e.m.

https://doi.org/10.1038/s41551-025-01487-5

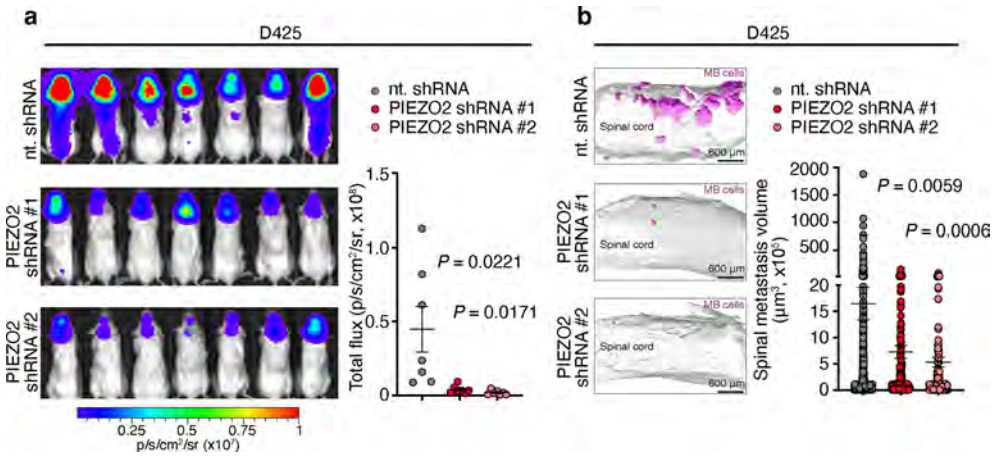

Extended Data Fig. 5 | Genetic targeting of PIEZO2 mitigates MB metastasis in D425 cells. a Bioluminescence imaging shows that genetic knockdown of PIEZO2 decreases the incidence of MB metastasis in D425 intracisternal xenograft model. Images were taken 14 days post implantation. Graph shows quantification of spinal radiance from $n = 7$ mice in each group. P values, two-sided unpaired t-test. Error bars, mean ± s.e.m. **b** Fluorescence imaging of optically cleared spinal cords shows that genetic knockdown of PIEZO2 reduces the burden of metastatic MB tumors along the spinal cords in DAOY intracisternal xenograft model. 3D reconstructions of the spinal cords (autofluorescence) and tumors (ZsGreen) are shown. Graph shows quantifications of spinal metastasis volume of $n = 917$ (nt. shRNA), $n = 183$ (PIEZO2 shRNA #1), and $n = 154$ (PIEZO2 shRNA #2) tumors from 7 mice in each group. P values, two-sided Welch's t-test. Error bars, mean ± s.e.m.

https://doi.org/10.1038/s41551-025-01487-5

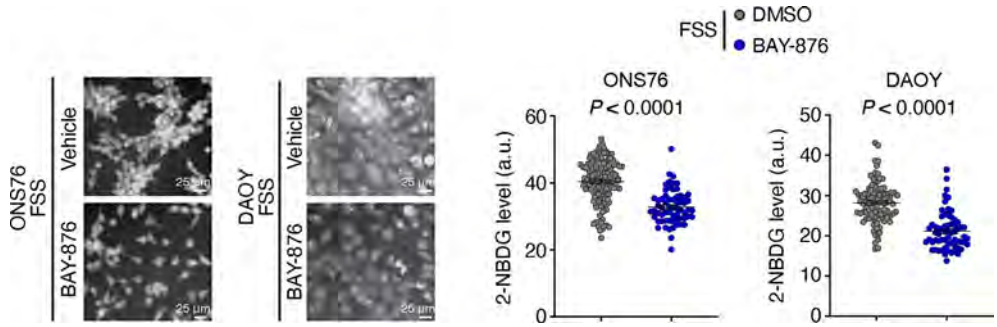

Extended Data Fig. 6 | GLUT1 inhibitor BAY-876 reduces glucose uptake in MB cells. BAY-876 treatment reduces 2-NBDG uptake of ONS76 and DAOY cells. Graphs show quantifications of 2-NBDG level in each cell from $n = 136$ (ONS76 DMSO), $n = 63$ (ONS76 BAY-876), $n = 101$ (DAOY DMSO), and $n = 64$ (DAOY BAY-876) cells from three independent replicates. P value, two-sided unpaired t-test. Error bars, mean ± s.e.m.

nature portfolio

Corresponding author(s): Xi Huang

Last updated by author(s): May 2, 2025

Reporting Summary

Nature Portfolio wishes to improve the reproducibility of the work that we publish. This form provides structure for consistency and transparency in reporting. For further information on Nature Portfolio policies, see our Editorial Policies and the Editorial Policy Checklist.

Statistics

For all statistical analyses, confirm that the following items are present in the figure legend, table legend, main text, or Methods section.

n/a	Confirmed	
☐	☒	The exact sample size (*n*) for each experimental group/condition, given as a discrete number and unit of measurement
☐	☒	A statement on whether measurements were taken from distinct samples or whether the same sample was measured repeatedly
☐	☒	The statistical test(s) used AND whether they are one- or two-sided *Only common tests should be described solely by name; describe more complex techniques in the Methods section.*
☒	☐	A description of all covariates tested
☐	☒	A description of any assumptions or corrections, such as tests of normality and adjustment for multiple comparisons
☐	☒	A full description of the statistical parameters including central tendency (e.g. means) or other basic estimates (e.g. regression coefficient) AND variation (e.g. standard deviation) or associated estimates of uncertainty (e.g. confidence intervals)
☐	☒	For null hypothesis testing, the test statistic (e.g. *F*, *t*, *r*) with confidence intervals, effect sizes, degrees of freedom and *P* value noted *Give P values as exact values whenever suitable.*
☒	☐	For Bayesian analysis, information on the choice of priors and Markov chain Monte Carlo settings
☒	☐	For hierarchical and complex designs, identification of the appropriate level for tests and full reporting of outcomes
☒	☐	Estimates of effect sizes (e.g. Cohen's *d*, Pearson's *r*), indicating how they were calculated

Our web collection on statistics for biologists contains articles on many of the points above.

Software and code

Policy information about availability of computer code

Data collection	LAS X (Leica, 1.4.4), Volocity (Quorum, 6.3.0), Zen Lightsheet 2014 (Zeiss), LivingImage (PerkinElmer, version 4.7.0).
Data analysis	Imaris (Oxford Instruments, version 10.1.1), Prism (GraphPad, version 10.0.3), ImageJ (version 1.54d), Volocity (Quorum, 6.3.0), LivingImage (PerkinElmer, version 4.7.0), Excel (Microsoft, version 2405). COMSOL Multiphysics 5.4 - the project file for CSF simulation is available at: https://github.com/XianShawn/CSF-Simulation. Hisat2 (v 2.2.1), Rsubread (v 2.18.0) - featureCounts, DESeq2 (v 1.44.0), clusterProfiler (v 4.12.0), ComplexHeatmap (v 2.20.0), Seurat (v 5.1.0) - NormalizeData, FindNeighbors, RunUMAP.

For manuscripts utilizing custom algorithms or software that are central to the research but not yet described in published literature, software must be made available to editors and reviewers. We strongly encourage code deposition in a community repository (e.g. GitHub). See the Nature Portfolio guidelines for submitting code & software for further information.

Data

Policy information about availability of data

All manuscripts must include a data availability statement. This statement should provide the following information, where applicable:

- Accession codes, unique identifiers, or web links for publicly available datasets
- A description of any restrictions on data availability
- For clinical datasets or third party data, please ensure that the statement adheres to our policy

The main data supporting the results in this study and source data are available within the paper and its Supplementary Information. The CSF flow simulation

project file is available at https://github.com/XianShawn/CSF-Simulation. Gene expression data (Affimetrix microarrays), tumor subtype information, and metastatic status for 763 primary medulloblastoma tumors of the SSH, WNT, Group 3, and Group 4 subtypes were downloaded from the Gene Expression Omnibus (GEO; GSE85217)73. Gene expression data for PIEZO1 and PIEZO2 expression analysis in SHH MB and normal cerebellum was downloaded from GEO; GSE124814. scRNA-seq expression data and metadata of human MB was retrieved from GEO; GSE119926. RNA-seq data of static and FSS-treated MB cells was deposited to GEO; (GSE288458). RNA-seq reads were aligned to GRCh38.

Research involving human participants, their data, or biological material

Policy information about studies with human participants or human data. See also policy information about sex, gender (identity/presentation), and sexual orientation and race, ethnicity and racism.

Reporting on sex and gender	Patient sex information is included in Supplementary Table 1.
Reporting on race, ethnicity, or other socially relevant groupings	Race, ethnicity, or other social groupings were not considered for this study.
Population characteristics	MRI images or tumor biopsy sections from medulloblastoma patients aged 3 months to 59 years were used for this study. Patient age information for each experiment is included in Supplementary Table 1.
Recruitment	T1-weighted contrast enhanced MRI images of 92 medulloblastoma patients in Xiangya Hospital were retrospectively collected for this study. Primary and metastatic medulloblastoma tumor biopsies from a patient in Xiangya Hospital were used for GLUT1 immunofluorescence.
Ethics oversight	MRI images: Xiangya Hospital Ethics Committee (#202404080). Immunofluorescence of GLUT1: Xiangya Hospital Ethics Committee (#2025010216).

Note that full information on the approval of the study protocol must also be provided in the manuscript.

Field-specific reporting

Please select the one below that is the best fit for your research. If you are not sure, read the appropriate sections before making your selection.

☒ Life sciences ☐ Behavioural & social sciences ☐ Ecological, evolutionary & environmental sciences

For a reference copy of the document with all sections, see nature.com/documents/nr-reporting-summary-flat.pdf

Life sciences study design

All studies must disclose on these points even when the disclosure is negative.

Sample size	No statistical method was used to predetermine sample size. However, sample sizes are consistent with those reported in previous publications (PMID: 36849558, 38514773).
Data exclusions	No data were excluded from the analyses.
Replication	All in vivo experiments were performed using at least 3 animals in each group. The patient medulloblastoma staining results are from matched primary and metastatic tumor sections from one patient. The number of independent replicates for each experiment are described in the corresponding figure legend. All attempts at replication yielded consistent results.
Randomization	For all mouse xenograft experiments, mice of same sex and comparable age and body weight were randomly assigned into experimental groups. For the intrathecal BAY-876 treatment experiment, bioluminescence imaging was performed prior to drug treatment and mice with comparable radiance signal were split into vehicle and treatment groups. For zebrafish xenografts, control and ccdc151 fish were injected at random, and the genotypes were determined subsequently.
Blinding	Blinding was applied for imaging of cleared spinal cords, quantification of glucose uptake, cell clustering, and immunofluorescence intensity. Where blinding was not applied, quantification was performed using software calculated automatic thresholds and standardized regions-of-interest across experimental groups.

Reporting for specific materials, systems and methods

We require information from authors about some types of materials, experimental systems and methods used in many studies. Here, indicate whether each material, system or method listed is relevant to your study. If you are not sure if a list item applies to your research, read the appropriate section before selecting a response.

Materials & experimental systems

n/a	Involved in the study
☐	☒ Antibodies
☐	☒ Eukaryotic cell lines
☒	☐ Palaeontology and archaeology
☐	☒ Animals and other organisms
☒	☐ Clinical data
☒	☐ Dual use research of concern
☒	☐ Plants

Methods

n/a	Involved in the study
☒	☐ ChIP-seq
☒	☐ Flow cytometry
☐	☒ MRI-based neuroimaging

Antibodies

Antibodies used

For F-actin staining, phalloidin (1:200, Invitrogen #A12379) was used. For immunofluorescence, the primary antibodies used were STEM121 (1:50; Takara #Y40420), rabbit anti-ColIV (1:100; BioRad #2150-1470), rabbit anti-GLUT1 (1:200; Sigma-Aldrich #07-1401), rabbit anti-phospho-myosin light chain 2 (1:100; Cell Signaling Technology #3671S), mouse anti-phospho-myosin light chain 2 (1:100; Cell Signaling Technology #3675S), rabbit anti-phospho-FAK (Tyr397) (1:100; Invitrogen #44-625G), and rabbit anti-caveolin-1 (1:100; Cell Signaling Technology #3267). The secondary antibodies used were Alexa Fluor 488 donkey anti-mouse IgG (1:200-400; Jackson Immunoresearch #715-545-151), Alexa Fluor 594 donkey anti-rabbit IgG (1:200-400; Jackson Immunoresearch #711-585-152), Alexa Fluor 647 donkey anti-mouse IgG (1:200-400; Jackson Immunoresearch #715-606-151) and Alexa Fluor 647 donkey anti-rabbit IgG (1:200-400; Jackson Immunoresearch #711-605-152). For zebrafish staining, primary antibody used was mouse anti-human nuclear antigen antibody (1:250; Thermo Fisher Scientific #MSM3-99-P0) and secondary antibody used was Alexa Fluor 488 donkey anti-mouse IgG (1:250; Jackson Immunoresearch #715-545-151).

Validation

All antibodies were purchased from the vendors listed above. All antibodies were used as validated by the manufacturer for their specific assay:
Phalloidin (Invitrogen #A12379) was validated for the fluorescence microscope, flow cytometer, confocal microscope, compatible with FITC/GFP filter sets
STEM121 (Takara #T40420) was validated for the localization, quantification, and/or characterization of engrafted cells of human origin by immunohistochemistry and immunofluorescence. It reacts with a human cytoplasmic protein expressed in brain, liver, pancreas, and CNS cells; the antibody does not cross-react with brain tissue or cell extracts from mouse, rat, or cynomolgous monkey.
Rabbit anti-ColIV (BioRad #2150-1470) was validated for use in ELISA, immunofluorescence, immunohistology - frozen, and immunohistology - paraffin. It reacts with mouse ColIV, and has cross reactivity with orangutan, rat, and human ColIV.
Rabbit anti-GLUT1 (Sigma-Aldrich #07-1401) was validated for use in immunocytochemistry, immunohistochemistry, and western blot. It was tested to react with human GLUT1 and predicted to react with mouse GLUT1 by homology.
Rabbit anti-phospho-myosin light chain 2 (Cell Signaling Technology #3671S) was validated for use in western blot and immunofluorescence, and reacts with human, mouse, rat, and drosophila melanogaster protein.
Mouse anti-phospho-myosin light chain 2 (Cell Signaling Technology #3675S) was validated for use in western blot and immunofluorescence, and reacts with human, mouse, rat, bovine, and pig protein.
Rabbit anti-phospho-FAK (Tyr397) (Invitrogen #44-625G) was validated for use in western blot and immunocytochemistry. It has been used for immunohistochemistry in 11 publications. It reacts with chicken, drosophila melanogaster, human, mouse, rat, and xenopus protein.
Rabbit anti-caveolin-1 (Cell Signaling Technology #3267) was validated for use in western blot, immunoprecipitation, immunohistochemistry, immunofluorescence, and flow cytometry. It reacts with human, mouse, rat, hamster, monkey, bovine, and dog Caveolin-1.
Mouse anti-human nuclear antigen antibody (Thermo Fisher Scientific #MSM3-99-P0) was validated for use in immunohistochemistry, immunocytochemistry, flow cytometry, and immunoprecipitation. It reacts with human and non-human primate nuclei and was validated not to react with mouse, rat, or chicken nuclei.
All secondary antibodies (Alexa Fluor 488 donkey anti-mouse IgG (1:200-400; Jackson Immunoresearch #715-545-151), Alexa Fluor 594 donkey anti-rabbit IgG (1:200-400; Jackson Immunoresearch #711-585-152), Alexa Fluor 647 donkey anti-mouse IgG (1:200-400; Jackson Immunoresearch #715-606-151), Alexa Fluor 647 donkey anti-rabbit IgG (1:200-400; Jackson Immunoresearch #711-605-152)) were validated for binding specificity using immunoelectrophoresis and/or ELISA. Each antibody has over 100 references with use in immunofluorescence.

Eukaryotic cell lines

Policy information about cell lines and Sex and Gender in Research

Cell line source(s)

Human medulloblastoma cell lines ONS76, DAOY, and D425 were a gift from Dr. Michael Taylor. ONS76 cells (RRID: CVCL_1624) and D425 cells (RRID: CVCL_1275) were originally acquired from the source labs (Yamada et al. 1989 No To Shinkei PMID: 2818910, Bigner et al. 1990 Cancer Research PMID: 2180567). DAOY cells (RRID: CVCL_1167) were originally purchased from ATCC (#HTB-186).

Authentication

ONS76 and D425 cells were authenticated by short tandem repeat testing. DAOY cells were not authenticated.

Mycoplasma contamination

ONS76 and DAOY cells were tested negative for mycoplasma by DAPI staining. D425 cells were tested negative for mycoplasma by PCR testing.

Commonly misidentified lines (See ICLAC register)	No cell line is listed in the database of commonly misidentified cell lines maintained by the International Cell Line Authentication Committee and National Center for Biotechnology Information BioSample.

Animals and other research organisms

Policy information about studies involving animals; ARRIVE guidelines recommended for reporting animal research, and Sex and Gender in Research

Laboratory animals	Female NOD scid gamma (J#5557) mice of 8-12 weeks of age were used. ccdc151(ts272) zebrafish were used
Wild animals	No wild animals were used.
Reporting on sex	All mice used were female. Zebrafish sex was not reported since they were used in the juvenile stage.
Field-collected samples	No field-collected samples were used.
Ethics oversight	Mouse procedures followed the Animals for Research Act of Ontario and the Guidelines of the Canadian Council on Animal Care, as approved by the TCP Animal Care Committee (protocol 27-0288H). Zebrafish were raised in accordance with Canadian Council on Animal Care (CCAC) guidelines and all zebrafish experiments were approved under an Animal Use Protocol established with the Animal Care Committee at the Hospital for Sick Children Research Institute (AUP #1000065704).

Note that full information on the approval of the study protocol must also be provided in the manuscript.

Plants

Seed stocks	This study did not involve plants.
Novel plant genotypes	This study did not involve plants.
Authentication	This study did not involve plants.

Magnetic resonance imaging

Experimental design

Design type	This is a retrospective observational study.
Design specifications	T1-weighted contrast-enhanced images of MB patients were selected for analysis.
Behavioral performance measures	n/a

Acquisition

Imaging type(s)	T1-weighted contrast-enhanced structure images
Field strength	For all patients, 3.0 T or 1.5 T field strength was used.
Sequence & imaging parameters	For CSF ventricular flow simulations, images of patient 1 and patient 5 were acquired from 3.0 T TOSHIBA MEC MRT200SP3. For T1-weighted contrast-enhanced structure images, TR time was 1800 ms, TE time was 15 ms, flip angle was set at 90, and slice thickness was 5 mm. Images of patient 2, 3, 4, 6, 8 and 10 were acquired from 1.5 T Aera from SIEMENS. For T1-weighted contrast-enhanced structure images, TR time was 400 ms, TE time was 11 ms, flip angle was set at 90, and slice thickness was 5 mm. Images of patient 7 and patient 9 were acquired from 3.0 T Signa HDxt from GE MEDICAL SYSTEMS. For T1-weighted contrast-enhanced structure images, TR time was 1711.89 ms, TE time was 26.18 ms, flip angle was set at 90, and slice thickness was 5 mm. Gadolinium was used for contrast agent. For spinal metastasis quantification, all MRIs were acquired using TOSHIBA MEC MRT200SP3, SIEMENS Sonata, Prisma, or Aera, GE MEDICAL SYSTEMS Signa or MR750w, or ALLTECH MEDICAL Centauri. Magnetic field strength used was 3.0 or 1.5 T. TR time was between 250-3002 ms. TE time was between 2.67 to 119.24 ms. Flip angle was 8, 12, 70, 75, 90, 111, or 142. Slice thickness was 5 mm for all patients, except for patients 20, 44, 45, 53, 60, 61, 69, and 87. For these patients, slice thickness was 1, 4, 1, 1, 4, 4, 3, 4, respectively. Gadolinium was used for contrast agent.
Area of acquisition	Whole brain for CSF ventricular flow simulations. Whole brain and spinal cord for spinal metastasis quantification.

Diffusion MRI ☐ Used ☒ Not used

Preprocessing

Preprocessing software: n/a

Normalization: n/a

Normalization template: n/a

Noise and artifact removal: n/a

Volume censoring: n/a

Statistical modeling & inference

Model type and settings: n/a

Effect(s) tested: n/a

Specify type of analysis: ☒ Whole brain ☐ ROI-based ☐ Both

Statistic type for inference: n/a

(See Eklund et al. 2016)

Correction: n/a

Models & analysis

n/a	Involved in the study
☒	☐ Functional and/or effective connectivity
☐	☒ Graph analysis
☒	☐ Multivariate modeling or predictive analysis

Graph analysis

A computational model was developed using COMSOL Multiphysics 5.4 to simulate the CSF within a tumor-obstructed conduit43. The 2D simulation model was built with CSF conduit geometries as previously shown43. A spherical blockage mimicking tumor was added to the CSF conduit at the cervicomedullary junction, taking up the conduit space froorm 0% up to 95%. The zero-displacement boundary condition was imposed at the surface of the CSF conduit. The CSF within the conduit was assigned to be moving liquid, with density of 1000 kg/m33, viscosity of 0.00103 Pa·s, and Poisson ratio of 0.49. The inlet was defined within the lateral ventricle, whereas the outlet was defined in the 4th ventricle. The mass flow inlet boundary condition with bulk production of 500 mLl/day (i.e., 6.25×10−6 kg/s) was used to mimic patient CSF flow. The COMSOL default mesh was used. The shear stress on the CSF conduit, the pressure, and the flow velocity within the conduit were recorded.